Atmos. Chem. Phys. Discuss., 10, 20673–20727, 2010
www.atmos-chem-phys-discuss.net/10/20673/2010/
doi:10.5194/acpd-10-20673-2010

Atmospheric Chemistry and Physics Discussions

Aerosol direct radiative forcing during Sahara dust intrusions in the Central Mediterranean

M. R. Perrone, A. Bergamo, and V. Bellantone

CNISM, Dipartimento di Fisica, Università del Salento, LECCE, Italy

Received: 11 June 2010 – Accepted: 9 August 2010 – Published: 31 August 2010

Correspondence to: M. R. Perrone (perrone@le.infn.it)

Published by Copernicus Publications on behalf of the European Geosciences Union.

Abstract

The clear-sky, instantaneous Direct Radiative Effect (DRE) by all and anthropogenic particles is calculated during Sahara dust intrusions in the Mediterranean basin, to evaluate the role of anthropogenic particle's radiative effects and to obtain a better estimate of the DRE by desert dust. The clear-sky aerosol DRE is calculated by a two stream radiative transfer model in the solar (0.3–4 µm) and infrared (4–200 µm) spectral range, at the top of the atmosphere (ToA) and at the Earth's surface (sfc). Aerosol optical properties by AERONET sun-sky photometer measurements and aerosol vertical profiles by EARLINET lidar measurements, both performed at Lecce (40.33° N, 18.10° E) during Sahara dust intrusions occurred from 2003 to 2006 year, are used to perform radiative transfer simulations. Instantaneous values at 0.44 µm of the real (n) and imaginary (k) refractive index and of the of aerosol optical depth (AOD) vary within the 1.33–1.55, 0.0037–0.014, and 0.2–0.7 range, respectively during the analyzed dust outbreaks. Fine mode particles contribute from 34% to 85% to the AOD by all particles. The complex atmospheric chemistry of the Mediterranean basin that is also influenced by regional and long-range transported emissions from continental Europe and the dependence of dust optical properties on soil properties of source regions and transport pathways, are responsible for the high variability of n, k, and AOD values and of the fine mode particle contribution. Instantaneous all-wave (solar+infrared) DREs that are negative as a consequence of the cooling effect by aerosol particles, span the – (32–10) Wm^{-2} and the – (44–20) Wm^{-2} range at the ToA and surface, respectively. The instantaneous all-wave DRE by anthropogenic particles that is negative, varies within – (13–7) Wm^{-2} and – (18–11) Wm^{-2} at the ToA and surface, respectively. It represents from 41% up to 89% and from 32% up to 67% of the all-wave DRE by all particles at the ToA and surface, respectively during the analysed dust outbreaks. A linear relationship to calculate the DRE by natural particles in the solar and infrared spectral range is provided.

ACPD
10, 20673–20727, 2010

1 Introduction

Large quantities of African dust are carried into the Mediterranean basin every year and as a consequence mineral dust is among the major aerosol components over the Mediterranean. The Direct Radiative Effect (DRE) by mineral dust is complex (Sokolik et al., 2001). Sign and magnitude of the dust DRE are controlled by dust optical properties, which depend on dust size distribution and dust refractive index. The latter depends on mineral composition and particle mixing state, which might vary regionally due to potentially different soil properties of dust source regions (Tegen, 2003). Desert dust absorbs at ultraviolet, visible, and infrared wavelengths and the African dust transport is driven by complex wind fields: the vertical structure of the dust layers reflects that complexity (e.g. Hamonou et al., 1999; di Sarra et al., 2001; De Tomasi et al., 2003). Hence, the presence of dust particles in the atmosphere can lead to either a cooling or a warming effect, depending on properties such as single-scattering albedo, altitude of the layer, and albedo of the underlying surface. According to Balkanski et al. (2007), over bare surfaces with a large surface albedo (>0.3) the mineral aerosols will always warm the atmosphere column. Over dark surfaces such as oceans and deciduous forests, where surface albedo (α) is less than 0.15, the effect of the mineral aerosols is similar to sulphates since it cools the atmospheric column. Over surface albedos in the intermediate range, $0.15 < \alpha < 0.30$, the sign of the forcing depends mainly on two factors, the size distribution and the mineralogical composition which both determine the single scattering albedo of the particles. Therefore the net radiative impact (sum of solar and long-wave) exhibits large regional variations, and this explains why the global mean is difficult to estimate: modeling studies and satellite retrievals do not agree on the amplitude and/or sign of the direct radiative perturbation from dust (Balkanski et al., 2007).

Physical and optical properties of the Saharan dust aerosol measured by the Met Office C-130 during the Saharan Dust Experiment (SHADE) have been used by Haywood et al. (2003) to calculate the instantaneous DRE by dust. They found that the

ACPD
10, 20673–20727, 2010

DRE at the top of the atmosphere (ToA) ranged from −44 to −129.2 Wm^{-2} in the solar spectrum as the AOD at 0.55 µm varied from 0.48 to 1.48. Hence, their results suggested that the Saharan dust aerosol exerts the largest local and global DRE of all aerosol species and should be considered explicitly in global radiation budget studies. Results on the DRE of Saharan dust from measurements at the Lampedusa Island, in two days of July 2002 (14 and 16) have also been reported by Meloni et al. (2003). They found that the instantaneous DRE over the 0.29–0.80 µm spectral range varied within the – (1.2–6.2) Wm^{-2} and the – (12.3–25.0) Wm^{-2} range at the ToA and surface, respectively for AODs at 0.42 µm spanning the 0.23–0.26 range. Several recent studies (e.g. Mallet et al., 2009; Raut and Chazette, 2008) have mainly investigated the dust DRE over African deserts.

The instantaneous DRE by all (anthropogenic plus natural) and anthropogenic aerosols from measurements at Lecce (40.33° N, 18.10° E), in southeastern Italy, during Sahara dust intrusion events, monitored from 2003 to 2006 year, is investigated in this paper to further contribute to the characterization of the direct radiative forcing by desert dust over the central Mediterranean: one of the most sensitive areas to climate change. Dust particles that are usually advected over the central Mediterranean at altitudes larger than 1.5 km (Papayannis et al., 2008) from ground, add to the pre-existing background aerosol and can affect the whole aerosol load up to ground (Bellantone et al., 2008; Pavese et al, 2009). Instantaneous DREs are calculated in this study by a two-stream radiative transfer model (Tafuro et al., 2007; Bergamo et al., 2008a, b) in the solar (0.3–4 µm) and infrared (4–200 µm) spectral range, at the top of the atmosphere (ToA) and at the surface (sfc): the ToA forcing is important to local and global radiation budgets, the sfc-forcing is important to surface heating and water evaporation (Bates et al., 2006).

Section 2 provides a brief description of the two stream radiative transfer model and of input data. The applied methodology to detect dust intrusion events over the monitoring site is outlined in Sect. 3, where two study cases are analyzed in more details. The applied methodology for DRE estimates by all (anthropogenic plus natural)

ACPD
10, 20673–20727, 2010

and anthropogenic particles is illustrated in Sect. 4, where results for one study case are also reported. Main results on instantaneous aerosol properties and corresponding DREs referring to all investigated dust outbreaks are analyzed and discussed in Sect. 5. Summary and conclusion are in Sect. 6.

2 The two-stream radiative transfer model and input data

Radiation Transfer Models (RTMs) are commonly used to compute aerosol radiative effects and the procedure to calculate the radiation field for a given distribution of aerosol optical properties is at the heart of all RTMs (Mayer and Kylling, 2005). The calculation procedure ranges from a variety of parameterizations and approximations to sophisticated and accurate solutions of the three-dimensional radiative transfer equation. A comparative study of four methods for solving the radiative transfer equation is reported in Kay et al. (2001). Most of the radiative transfer equation solvers are plane-parallel, that is, they neglect the Earth's curvature and assume an atmosphere of parallel homogeneous layers. Some of the solvers include a so-called pseudo-spherical correction which treats the direct solar beam in spherical geometry and the multiple scattering in plane-parallel approximation (Dahlback and Stamnes, 1991). The widely used UVSPEC radiation transfer model (Mayer et al., 1997) allows the choice of one among three methods for the solution of the radiative transfer equation: the two stream approximation (Meador and Weaver, 1980) that is one of the simplest techniques to solve the radiative transfer equation, the discrete ordinate method (DISORT) for plane-parallel atmosphere (Stamnes et al., 1988), and the pseudo spherical approximation of DISORT (SDISORT). The proper accounting for the spectral dependence of the aerosol optical properties is also important in RTMs. Aerosol optical properties vary with wavelength (λ) and as a consequence their interaction with radiation is very sensitive to λ. Recent studies showed that both to neglect completely the spectral dependence and consider only specific spectral range of aerosol properties can be important error sources (Zhou et al., 2005; Hatzianastassiou et al., 2007).

ACPD
10, 20673–20727, 2010

Measurement-based aerosol properties are used in this study to initialize the two-stream radiative transfer model. A detailed description of the used two-stream RTM is given in Tafuro et al. (2007). Twenty homogeneous plane-parallel atmospheric layers are used in the model to account for the changes with altitude of atmospheric parameters and components (e.g. pressure, temperature, gases, and particle distributions), and radiative fluxes are determined in the solar (0.3–4 µm) and infrared (4–200 µm) spectral region. Eight solar and twelve infrared subbands are considered to properly account for the spectral dependence of atmospheric particle properties: the optical properties (extinction, single-scattering albedo, and asymmetry factor) of the atmospheric particles remain constant in each of the 20 subbands. Centers of the eight solar subbands are at: 0.35 µm, 0.45 µm, 0.55 µm, 0.65 µm, 1.00 µm, 1.6 µm, 2.2 µm, and 3.0 µm. Centers of the twelve IR subbands are at: 4.25 µm, 5.35 µm, 6.25 µm, 7.35 µm, 8.75 µm, 10.30 µm, 11.75 µm, 13.90 µm, 17.20 µm, 24.30 µm, 37.00 µm, and 80.00 µm. Absorption of trace gases (H_2O, O_3, CO_2, CO, N_2O, and CH_4) is represented by *I* exponential terms in each of the 20 spectral subbands, with *I* varying within the 1–12 range. Thus, 20 applications of the radiative transfer model are required to account for the solar and infrared spectral dependence of each trace gas (Tafuro et al., 2007).

Input data include instantaneous size distributions and real (n) and imaginary (k) refractive indices from AERONET sun-sky photometer measurements (Holben et al., 1998) performed at Lecce during Sahara dust intrusion events that have occurred from 2003 to 2006. In particular, cloud-screened and quality-assured AERONET retrievals (level 2.0) from the Version 2 (V2) inversion algorithm are used in this study. For the near-infrared region of the solar spectrum, the AERONET refractive indices extracted for the wavelength at 1.02 µm are applied. n and k values for mineral aerosol (Sokolik and Toon, 1998) are used in the far infrared spectral region (Table 1). MIE calculations (assuming a spherical particle shape) are applied to translate the data on size, concentration, and refractive indices into AODs (a measure of the magnitude of the aerosol extinction due to scattering and absorption), single scattering albedo (SSA) values

ACPD
10, 20673–20727, 2010

(a measure of the relative importance of absorption and scattering), and asymmetry-factor (g) values (a measure of the angular distribution of the scattering radiation). AOD, SSA, and g represent the major used parameters in aerosol DRE simulations.

Surface albedo values are based on the ones assumed for Lecce in the AERONET inversion code at the wavelengths corresponding to sky radiance measurements. A surface emissivity of 0.96 is assumed in the far-infrared.

Lidar measurements performed within the European Aerosol Research Lidar Network-EARLINET (e.g. Matthias et al., 2004) are used to characterize the aerosol vertical distribution. Data from a ground-based meteorological station operating at the AERONET site are used to define density, pressure, temperature, and water vapor at the surface. Then, radiosonde measurements (see also http://esrl.noaa.gov/raobs/) at the meteorological station of Brindisi that is 40 km north-west of Lecce are used to define vertical profiles of density, pressure, temperature, and water vapor from 1 up to 20 km altitude. Above 20 km of altitude, vertical profiles of density, pressure, temperature, and water vapor are extended with corresponding mid-latitudes standard atmosphere data provided by the Air Force Geophysics Laboratory (AFGL) for autumn-winter and spring-summer months. The Rayleigh scattering due to atmospheric molecules is taken into account (Tafuro et al., 2007).

Vertical profiles of oxygen, ozone, and well mixed trace-gases (N_2O, CO_2, CO and CH_4) are prescribed by the US Air Force Geophysics Laboratory (AFGL) standard atmosphere for mid-latitude (30°–60° N) summer and winter with interpolations for the transitional seasons. Trace-gas concentrations in conjunction with pre-defined absorption coefficients are used to compute gas absorption.

3 Detection of dust events: methodology

Dust particles are usually advected over the central Mediterranean and European regions at altitudes larger than 1.5 km from ground and add to the pre-existing aerosol. Then, the coexistence of lofted Sahara dust plumes over European areas with

ACPD
10, 20673–20727, 2010

significant anthropogenic aerosol sources in the boundary layer (Pérez et al., 2006) does not allow their accurate separation, when examining satellite or ground-based columnar measurements. Polarization-sensitive lidar systems are the best tool to infer dust intrusion events and to monitor the structure of lofted dust plumes, since they allow tracing the vertical distribution of the aerosol optical properties. A multistep approach has been adopted in this study to properly detect dust intrusion events over Lecce. More specifically, a polarization sensitive lidar system whose light source is a XeF excimer laser operating a 0.351 µm has been used in step (1), to retrieve aerosol backscatter coefficient (β(z)) and depolarization ratio (δ(z)) vertical profiles of aerosol layers (De Tomasi et al., 2006). δ(z) is the ratio of cross-polarized to parallel-polarized backscatter coefficient and takes a value of 0.014 in a pure molecular atmosphere and generally higher values in presence of non spherical particles such as desert dust particles. Depolarization ratios up to 50% and 56% were retrieved over Etna by Tafuro et al. (2006) and over Lampedusa by Meloni et al. (2004), respectively for the presence of Sahara dust particles. However, significantly lower δ(z) values are retrieved during low intensity dust outbreaks. Hence, while backscatter coefficient profiles allow tracing the vertical distribution of the whole aerosol load, δ(z) profiles can allow inferring the location of aerosol layers with a larger content of non-spherical particles. In addition to step 1, aerosol products by AERONET sun/sky photometer measurements collocated in space and time with lidar measurements have been used in step (2) to support the presence dust particles inferred by lidar measurements. In particular, the AERONET sphericity parameter, the Angstrom coefficient, computed from AOD values at 0.44 µm and 0.87 µm, the columnar volume size distribution, and the fine mode fraction have been used. Typical Å values range from 1.5 for aerosol dominated by accumulation mode particles, to nearly zero for large dust particles (e.g. Tafuro et al., 2006). The new AERONET retrieval scheme (Dubovik et al., 2006) considers aerosol particles made by a mixture of polydisperse, randomly oriented, homogeneous spheroids with a fixed distribution of aspect ratios and accordingly, it provides the fraction (in percentage) of spherical particles (sphericity parameter). Therefore, the sphericity parameter

ACPD
10, 20673–20727, 2010

(S) gets smaller values as the contribution of non spherical dust particle increases. The AERONET fine mode fraction also decreases as the contribution of coarse mode particles such as desert particles increases. In addition to steps 1 and 2, analytical back trajectories have been used in step (3) to identify the aerosol source region and hence the occurrence of a dust transport over the monitoring site. To this end, 7-day analytical back trajectories by NASA GSFC (http://croc.gsfc.nasa.gov/aeronet/index.html) have been used. Finally, true-color satellite images by the MODerate Resolution Imaging Spectroradiometer – MODIS (http://modis.gsfc.nasa.gov/; King et al., 1992) have been used in step 4 to further support the dust transport over the monitoring site.

Results for two study cases are presented in the following sub sections to better illustrate the methodology for the detection of dust outbreaks over Lecce. In particular, the dust outbreaks occurred on 5 July 2005 and on 22 June 2006 are analyzed: 5 July and 22 June dust events are representative over south-east Italy of typical weak and strong dust intrusion events, respectively.

3.1 5 July 2005 dust event

Figure 1a–d (solid lines) shows the aerosol backscatter coefficient profiles retrieved from polarization sensitive lidar measurements performed at Lecce on 5 July 2005 at different day hours (UTC). Grey dotted lines in Fig. 1b and d represent depolarization ratio vertical profiles. Depolarization ratio uncertainties are lower than 10%. The β(z) profile in Fig. 1a reveals the presence of a significant aerosol load up to ~1.5 km from ground, even if aerosol particles are detected up to higher altitudes. A well defined, additional aerosol layer extending from about 3.2 up to 4.1 km and characterized by δ(z) values slightly larger than 0.02 is revealed by lidar measurements performed from 08:44 up to 09:36 UTC (Fig. 1b). We also observe that the aerosol vertical distribution significantly varies with the time of the day (Fig. 1c–d) and that the aerosol column burden increases. In addition, δ(z) values in Fig. 1d (dotted line) indicate that non spherical particles contribute to the aerosol layer extending up to ~5 km from ground. Both the high variability of the aerosol vertical distribution that is usually observed during

ACPD
10, 20673–20727, 2010

dust outbreaks (Pavese et al., 2009) and δ(z) profiles suggest that the monitoring site is affected by the advection of non-spherical particles, since late morning.

Figure 1e shows the columnar volume size distribution retrieved from AERONET measurements at different day hours. The V2 AERONET retrieval provides volume particle size distribution in 22 logarithmically equidistant bins in the radius range 0.05–15 µm. We observe from Fig. 1e that the columnar volume size distributions retrieved from measurements performed in the early afternoon of 5 July, are significantly larger than the one retrieved at 04:53 UTC. These results are in accordance with the column burden increase revealed by lidar measurements. In addition, the bimodal structure of Fig. 1e spectra retrieved since 14:58 UTC indicates that along with fine mode particles, coarse-mode particles also significantly contribute to the aerosol burden. In fact, the Angstrom exponent that is equal to 2.0 at 04:53 UTC takes the 1.4 value at 14:58. In addition, the sphericity parameter that takes values spanning the 20–40% range on the afternoon of 5 July, also allows inferring the presence of non spherical particles in accordance with depolarization ratio measurements. Figure 2a–b shows the 7-day analytical back trajectories for the air masses reaching Lecce on 5 July, at 12:00 UTC. Analytical back trajectories are provided by NASA for each AERONET site, at eight distinct arrival pressure levels (950, 850, 700, 500, 400, 300, 250, and 200 hPa) and at two arrival times (00:00 and 12:00 UTC). The trajectories are based on a kinetic trajectory analysis using NASA GMAO assimilated gridded data. Pathways of the 950, 850, 700, and 500 hPa back trajectories are plotted in Fig. 2a. The altitude of each back trajectory as a function of time is shown in Fig. 2b. We observe from Fig. 2a that the 500 hPa back trajectory travels over north-west Africa before reaching the monitoring site. Conversely, the 950 and 850 hPa back trajectories cross northeastern Europe before reaching Lecce. MODIS true color images reveal that on 5 July the central Mediterranean is affected by Sahara dust (http://rapidfire.sci.gsfc.nasa.gov/realtime/single.php?T051861100; http://rapidfire.sci.gsfc.nasa.gov/realtime/single.php?A051811215). Therefore, back trajectories and MODIS images support the advection of Sahara dust particles over Lecce on 5 July 2005, in accordance with lidar and sun/sky photometer

ACPD
10, 20673–20727, 2010

measurements (Fig. 1). However, the anthropogenic pollution advected from north-eastern Europe is also likely responsible for the increase of the aerosol column burden revealed by Fig. 1 and more specifically for the fine mode particle contribution. The coexistence at different altitudes of air masses advected from different areas/sources is quite often observed over southeastern Italy (Santese et al., 2008).

3.2 22 June 2006 dust event

Figure 3a–e shows the aerosol backscatter coefficient profile $\beta(z)$ retrieved from lidar measurements performed on 22 June at different day hours (UTC). Grey dotted lines represent vertical profiles of the depolarization ratio. Figure 3a shows that the aerosol layer extends up to ~2.7 km at the early morning. Conversely, lidar measurements performed from 10:28 to 11:32 UTC reveal that the aerosol burden extends up ~6 km (Fig. 3b). Aerosols up to ~6 km have been detected by the lidar at least up to 16:37 UTC, in accordance with Fig. 3a–e. Dotted lines in Fig. 3a and b show that the depolarization ratio is of about 0.07 from about 0.5 to 2 km and of about 0.08 from 0.5 to 5.5 km, respectively. δ values (Fig. 3a–b) allow inferring the presence of non spherical particles and hence, likely, of desert dust particles. Moreover, the poor dependence of δ values on altitude revealed by Fig. 3a and b, suggests that non-spherical particles are well mixed in the whole aerosol layer. It is worth noting from Fig. 3c that rather high depolarization ratios ($\cong$0.4) are detected by lidar measurements at ~4.5 km of altitude. We believe that the high variability within few hours of the aerosol column burden and the larger $\beta(z)$ and $\delta(z)$ values revealed by Fig. 3c can likely be due to the advection of desert particles. Pathways of the 7-day analytical back trajectories reaching Lecce on 22 June (Fig. 2c–d) support last comment. We observe from Fig. 2c that the 700 and 500 hPa back trajectories originate over Mauritania and south-east Algeria, respectively and travel over north-west Africa before reaching the monitoring site. Conversely, the 950 and 850 hPa back trajectories cross Tunisia and north-east Algeria but, they spend a large fraction of the days over the central Mediterranean basin.

ACPD
10, 20673–20727, 2010

In addition to back trajectories and lidar measurements, aerosol products by AERONET sun/sky photometer measurements also support the presence of desert dust particles over Lecce. Figure 3f shows the columnar volume size distribution retrieved from AERONET measurements at 15:31 UTC (dotted line) and at 16:27 UTC (solid line). The bimodal structure of Fig. 3f spectra indicates that along with fine mode particles, coarse-mode particles also significantly contribute to the aerosol burden, which increases from 15:31 UTC to 16:27 UTC, in accordance with lidar measurements (Fig. 3d–e). The bimodal structure of the columnar volume size distributions of Fig. 3 is generally observed at Mediterranean AERONET sites during Sahara dust outbreaks, as it has been shown by Tafuro et al. (2006) and Fotiadi et al. (2006). However, the coarse mode in the bimodal distribution could also be attributed (at least to some extent) to maritime sea-salt aerosols (e.g. Fotiadi et al., 2006). The sphericity parameter that takes the value of 1.5 and 1.9% at 15:31 and 16:27 UTC, respectively and the Angstrom coefficient that takes the value of 0.46 and 0.52 at 15:31 and 16:27 UTC, respectively also support the advection of dust particles over Lecce. True colour MODIS images also reveal the presence of desert dust over south-eastern Italy.

4 Aerosol direct radiative effect estimates: methodology

Results on clear-sky aerosol DREs for 22 June 2006 are presented in the following subsections, as an example, to better illustrate the methodology to calculate instantaneous DREs by all (anthropogenic plus natural) and anthropogenic particles.

4.1 Study case: aerosol DREs on 22 June 2006

Instantaneous values at 0.44 µm of the real (n) and imaginary (k) refractive index retrieved from AERONET measurements at 15:31 UTC and at 16:27 UTC of 22 June 2006 are given in Table 2 in addition to AOD, Å, S, and α values calculated from AERONET data. Instantaneous columnar volume size distributions are plotted in Fig. 3f. As mentioned in Sect. 2, MIE calculations are applied in the RTM to translate input data (n, k, and size distributions) into AOD, SSA, and asymmetry-factor (g)

ACPD
10, 20673–20727, 2010

values: the main parameters generally used to understand the complex interaction of aerosols with radiation. Table 3 shows AOD, SSA, and g values at 0.55 µm retrieved by MIE calculations, in addition to corresponding values retrieved by the AERONET inversion algorithm (Dubovik et al., 2006). AERONET AOD, SSA, and g values retrieved at 0.44 and 0.675 µm, respectively have been averaged to calculate AOD, SSA, and g values at 0.55 µm. The differences between AERONET and corresponding Mie-code values are equal and smaller than the AERONET retrieval accuracy for AOD and SSA values, respectively. The AERONET retrieval accuracy is ±0.01 and ±0.03 for AOD and SSA values, respectively, according to Dubovik et al., 2002. Conversely, the differences between AERONET and Mie-code g values that are ≤0.05, are larger than the theoretical AERONET retrieval accuracy, which is equal ±0.02, according to Yu et al. (2006). This is probably due to the fact that MIE calculations consider particles to be spherical, while the AERONET inversion algorithm considers aerosol particles made by a mixture of polydisperse, randomly oriented, homogeneous spheroids. Mishchenko et al. (1997) have shown that the error in the asymmetry factor due to the non-sphericity of the particles is inferior to 7%.

AOD, SSA, and g values by the Mie's code, α values from Table 2, and the AOD fraction vertical profiles retrieved by the β(z) vertical profiles of Fig. 3e and d, have been used to calculate the clear-sky instantaneous aerosol DRE at 15:31 and 16:27 UTC. Instantaneous DRE values by the whole aerosol (DRE_t) at solar and infrared (IR) wavelengths, and at the ToA and surface, respectively are given in Table 4, in addition to the surface net flux (F_{sfc}) in the solar and IR spectral range, respectively. Table 4 shows that aerosol DREs at solar wavelengths are negative at the ToA and surface since aerosol particles determine a planetary and surface cooling. In particular, the DRE at the surface by all particles ($DRE_{t,sfc}$) is 2.7 and 1.5 larger than that at the ToA at 15:31 and 16:27 UTC, respectively, in accordance with previous studies (e.g. Tafuro et al., 2007; Bergamo et al., 2008b; Meloni et al., 2003). It is also worth noting that the surface DRE decreases in magnitude from 15:31 to 16:27 UTC, while it increases at the ToA. The larger contribution of fine mode particles and the smaller k value found

ACPD
10, 20673–20727, 2010

at 16:27 UTC contribute to this last result. Aerosol DREs at infrared wavelengths are positive and in particular, the aerosol IR-DRE offsets the solar-DRE by 8.5% and of 17% at the ToA and surface, respectively at 15:31 UTC. The aerosol IR-DRE offsets the solar-DRE by 7.2% and of 22% at the ToA and surface, respectively at 16:27 UTC. These last results reveal the significant role of the IR-DRE during dust intrusion events.

4.2 Comparisons of modeled fluxes with measured and AERONET solar fluxes

Instantaneous solar fluxes by the model (open dots) are compared in Fig. 4 with corresponding solar flux estimates (open boxes) by AERONET to test the accuracy of our model in the solar spectral range. The radiative transfer model used within AERONET to estimate broadband radiative fluxes and aerosol DREs is described in Garcia et al. (2008), where validation tests by ground-based broadband measurements are also reported. The AERONET broadband fluxes are calculated by spectral integration in the range from ~0.3 to 2.8 µm using more than 200 size sub-intervals. The simulation relies on the retrieved complex refractive index at operational wavelengths of CIMEL sun/sky photometers and the retrieved aerosol size distributions. The spectral integration employs real and imaginary parts of refractive index that are interpolated/extrapolated from the values of complex refractive index retrieved at AERONET wavelengths. Similarly, spectral dependence of surface reflectance is also interpolated/extrapolated from surface albedo values assumed in the retrieval on the wavelengths of the sun/sky photometer. Similarly, to the AERONET retrieval approach, flux calculations account for absorption and multiple scattering effects using the Discrete Ordinate DISORT approach (Stamnes et al., 1988). The integration of atmospheric gaseous absorption and molecular scattering effects are conducted using developments employed in the Global Atmosphere ModEl (GAME) code (Dubuisson et al., 1996). Thus, the AERONET calculation of broadband radiation is focused on accurate accounting for the spectral dependence of atmospheric gases, aerosol optical properties and surface albedo used as input. It is worth noting from Fig. 4, that the AERONET solar flux values at the surface are in satisfactory accordance with our model results (differences are smaller

ACPD
10, 20673–20727, 2010

than 1%), despite the different methodology used to solve the radiative transfer equation (Kay et al., 2001) and the poorer spectral resolution of our model. We believe that these results support the accuracy of our model in the solar spectral range.

Modeled all-wave (solar+IR) fluxes at the surface (full dots) are compared in Fig. 4 to broadband all-wave flux measurements at the surface (solid line) by a net radiation transducer (p056 RADNT, by SIAP+MICROS S.r.l., Italy) characterized by 1.5% accuracy, which is routinely used at the ISAC-CNR Department of Lecce (www.basesperimentale.le.isac.cnr.it), to monitor broadband all-wave fluxes in the 0.3-30 µm spectral range, with two hemispheric (up and down) sensors, which do not allow separating solar and IR component. The net radiation transducer is located few hundred meters away from the AERONET sun/sky radiometer site. Figure 4a reveals that measured all-wave fluxes are in satisfactory accordance with modeled values: modeled all-wave fluxes are 15% and 5% larger than measured all-wave fluxes at 15:31 and 16:27 UTC, respectively. We believe that these last results are encouraging and support the appropriateness of our model in the (solar+IR) spectral range.

4.3 Direct radiative effects by anthropogenic particles on 22 June 2006.

Volume size distributions of Fig. 3f indicate that along with coarse-mode particles, fine-mode particles, which are mainly due to anthropogenic aerosol, also contribute to the aerosol burden of 22 June 2006. The anthropogenic aerosol contribution is associated in this paper with the number concentration of fine-mode aerosol $N_f(r)$ provided by AERONET, in accordance to Bergamo et al. (2008a). Potential anthropogenic contributions to the coarse-mode aerosol are ignored. In particular, only a fraction f of $N_f(r)$ is considered of anthropogenic origin in accordance with the following relationship

$$N_a(r) = f \times N_f(r) \quad (1)$$

where $N_a(r)$ is the number concentration of anthropogenic-only submicron aerosol particles. Monthly f–values relating to Lecce are given by Bergamo et al. (2008a) and are considered constant with particle size in the submicron fraction. f–values are based

ACPD
10, 20673–20727, 2010

on LMDzT3.3 (Reddy et al., 2005) global model-simulations (Schulz et al., 2006). In particular, inventories for global emissions of aerosols and pre-cursor gases for the years 2000 (current conditions) and 1750 (pre-industrial conditions) have been used in the General Circulation Model LMDzT3.3 to calculate f –values (Dentener et al., 2006, Stier et al., 2007).

MIE calculations are applied to translate the data on number concentration of anthropogenic aerosols (Eq. 1) into aerosol optical depth, single-scattering albedo, and asymmetry factor for anthropogenic particles: AOD_a, SSA_a, and g_a, respectively. Refractive indices are not considered dependent on particle size. A discussion on this last assumption is given in Bergamo et al. (2008a). AOD_f and AOD_a values at 0.55 µm by MIE calculations and for $f = 0.73$ are given in Table 4. It is worth noting that 38% of the AOD_t (Table 3) is due to anthropogenic particles at 15:31 and 16:27 UTC, respectively.

Simulated DRE values by anthropogenic particles (DRE_a) in the solar and infrared spectral range, and at the ToA and surface are given in Table 4. The solar ToA-DRE by anthropogenic particles ($DRE_{a,ToA}$) is 48% and 44% of the solar-ToA-DRE by all particles ($DRE_{t,ToA}$) at 15:31 and 16:27 UTC, respectively. Conversely, 28% and 33% of the solar-$DRE_{t,sfc}$ is due to anthropogenic particles at 15:31 and 16:27 UTC, respectively. The IR-DRE by anthropogenic particles is negligible at the ToA, whereas at the surface, it represents 10% and 13% of the of the IR-$DRE_{t,sfc}$ at 15:31 and 16:27 UTC, respectively. In conclusion, the results listed above highlight the role of anthropogenic particles during Sahara dust intrusion in the Mediterranean and allow inferring that on 22 June 2006, the all-wave (solar + IR) DRE by desert dust particles is less than 56% and 67% of the all-wave DRE by all particles at the ToA and surface, respectively. Recent studies (e.g. Bellantone et al., 2008; Carofalo et al., 2008) on the chemical composition of the ground-collected particulate matter have also revealed the significant contribution of anthropogenic particles during dust outbreaks over south-eastern Italy.

ACPD
10, 20673–20727, 2010

The above calculated DREs by anthropogenic particles depend on the accuracy of size distributions retrieved by the AERONET inversion algorithm. A discussion on this subject is given in the following Section.

4.4 Comments on the accuracy of AERONET size distributions

Aerosol size is a key parameter to separate natural from man-made aerosol and infer the anthropogenic contribution to the total aerosol load. Hence, the results reported in Sect. 4.3 depend on the accuracy of volume size distributions retrieved by the AERONET inversion algorithm. Dubovik et al. (2002) have shown that the error of the retrieved volume density changes as a nonlinear function of particle size, aerosol type, and actual values of the size distribution. In particular, for the intermediate particle size range ($0.1 \leq r \leq 7\,\mu m$), the retrieval errors do not exceed 10% in the maxima of the size distribution and may increase up to about 35% for the points corresponding to the minimum values. For the edges ($0.05 \leq r < 0.1\,\mu m$ and $7 < r \leq 15\,\mu m$) of the assumed particle size interval, the accuracy of the size distribution retrieval drops significantly and retrieval errors rise up to 80%–100%. It is worth mentioning that the AERONET inversion algorithm constrains particles with radius r larger than 15 µm to be absent. As a consequence of this assumption, the fine mode size distribution can be overestimated if large particles ($r > 15\,\mu m$) contribute to the aerosol column burden, according to Kleidman et al. (2005). More specifically, they have shown that when the fine mode fraction (η) takes values smaller than 0.6, the Dubovik inversion of sky radiances overestimates η for dust aerosol by 0.1–0.2 relative to the O'Neill method of inverting AERONET AOD spectra. The above reported comment suggests that the number concentration of fine-mode aerosol ($N_f(r)$) retrieved on 22 June 2006 by the AERONET inversion algorithm, is probably overestimated being $\eta < 0.5$. Then, we have assumed that $N_f(r)$ is overestimated by 40% to test on 22 June 2006, the sensitivity of the DRE by anthropogenic particles to AOD_a values. In particular, we have set, as an example

$$N_{f,cor}(r) = 0.6 N_f(r) \quad (2)$$

ACPD
10, 20673–20727, 2010

where $N_{f,cor}(r)$ is the corrected number concentration of fine-mode particles. Then, we have applied Eq. (1) to calculate $N_{a,cor}(r)$: the corrected number concentration of anthropogenic-only submicron aerosol particles. Mie calculations have been applied to get the corrected AOD (AOD_{cor}) by fine ($AOD_{f,cor}$) and anthropogenic ($AOD_{a,cor}$) particles (Table 4). We observe from Table 4 that $AOD_{f,cor}$ is 62% and 59% of AOD_f at 15:31 and 16:27 UTC, respectively. Then, the difference between $\eta = AOD_f / AOD_t$ and the corrected fine mode fraction $\eta_{cor} = AOD_{f,cor}/AOD_t$ is equal to 0.19 and 0.17 at 15:31 and 16:27 UTC, respectively (Kleidman et al., 2005). $AOD_{a,cor}$ is 50% and 58% of AOD_a at 15:31 and 16:27 UTC, respectively. Then, the solar DRE by the corrected estimate of anthropogenic particles ($DRE_{a,cor}$) decreases in magnitude of about 44% at the ToA and surface, respectively (Table 4). The IR-DRE by $AOD_{a,cor}$ decreases at the surface by 45%. These results besides showing the strong dependence of the DRE_a on the number concentration of fine-mode particles, reveal the need of accurate estimates of fine mode size distributions to properly evaluate DREs by anthropogenic particles. However, it is noteworthy that AERONET measurements and products are extensively used as the only ground truth in aerosol-related research.

5 Results on 2003–2006 dust outbreaks

The selected dust events are listed in Table 2, where AERONET instantaneous values of AOD, n, and k at 0.44 µm, of the Angstrom coefficient (0.44 µm/0.87 µm), the sphericity parameter, and of the solar surface albedo (α) are also given. A multistep approach based on polarization-sensitive lidar measurements, AERONET products, 7-day analytical back trajectories, and true-color MODIS images has been used to select dust intrusion events over Lecce, as we have outlined in Sect. 3.

ACPD
10, 20673–20727, 2010

5.1 Analysis of AERONET products during Sahara dust intrusions

Instantaneous columnar size distributions and n and k values by AERONET are used in the radiative transfer code to define aerosol properties. Figure 5a shows the instantaneous columnar volume size distributions retrieved by AERONET measurements performed on the selected dusty-days, to highlight main features of dusty-day volume size distributions. The largest coarse mode peak at ∼2.5 µm has been retrieved from measurements performed on 17 July 2003 at 04:59 UTC. The grey line in Fig. 5a represents the mean columnar volume size distribution obtained by averaging all instantaneous volume distribution profiles. Vertical error bars in Fig. 5a represent ±1 standard deviation from the average value and indicate the volume size distribution variability. The significant role of coarse-mode particles in dusty-days is clearly pointed-out by Fig. 5a, which reveals that the mean coarse mode distribution peaks at ≅2.2 µm. However, along with coarse-mode particles, fine-mode particles also contribute to the aerosol burden. In fact, the fine mode fraction η, i.e. the ratio between the fine-mode and the total optical depth at 0.55 µm spans the 0.34–0.79 range on the selected dusty days.

Instantaneous Å values versus AODs at 0.44 µm, retrieved during dusty-days are plotted in Fig. 5b. Different symbols are used to characterize different dusty-days. Å represents a good marker of dust outbreaks, as we have mentioned. We observe that instantaneous Å values span the 1.5–0.23 range. Nevertheless, data points relating to a given day vary within a rather small range. This result may indicate that aerosol microphysical properties are quite dependent on the dust event and less on the aerosol property changes during the day. Figure 5b shows that Å values become smaller as the AOD increases. Hence, coarse mode particles are responsible for the large AODs monitored during dust events. The rather high Å values retrieved during low-AOD dusty-days are probably due to the larger contribution of fine mode particles of local origin and/or long-range transported (Fig. 2a–b). Figure 6a and b show the scatterplot of n and k values versus the AOD at 0.44 µm, respectively. n and k instantaneous values vary within the 1.33–1.55 and 0.0037–0.014 range, respectively

ACPD
10, 20673–20727, 2010

during the monitored dust outbreaks and are quite dependent on the aerosol column burden, in accordance with Fig. 5b. The columnar averaged value ±1 SD of n and k is: $< n > = 1.48 \pm 0.01$ and $< k > = 0.007 \pm 0.002$ at AODs >0.45. Whereas, <Å> = 0.33 ± 0.07 for AODs >0.45 (Fig. 5b). These last results are in accordance with corresponding mean values reported by Tafuro et al. (2006). AERONET sun/sky photometer measurements performed at five different sites of the central Mediterranean during strong Saharan dust outbreaks, have been used by Tafuro et al. (2006) to calculate Å, n and k mean values. Hence, the $< n >$ and $< k >$ values of this paper at AODs (0.44 µm) >0.45, further more contribute to the definition of the mean aerosol properties in the Mediterranean basin, during strong dust intrusion events.

5.2 Modeled aerosol properties at 0.55 µm

Instantaneous AOD_t, SSA_t, and g_t values at 0.55 µm, recomputed by Mie calculations from AERONET-derived aerosol size distributions and refractive indices, are plotted in Fig. 7a–7c, respectively, as a function of the fine mode fraction η at 0.55 µm. Relative differences between AERONET and corresponding Mie-code values span the 6%–12%, 0.03%–3%, and 3%–7% range for AOD_t, SSA_t, and g_t, respectively. AERONET AOD_t, SSA_t, and g_t values retrieved at 0.44 and 0.675 µm, respectively have been averaged to calculate AERONET AOD_t, SSA_t, and g_t values at 0.55 µm.

Figure 7a shows that AOD_t values span the 0.19–0.64 range and increase as η values decrease, in accordance with Fig. 5b. g_t values that span the 0.61–0.70 range also increase as η values decrease (Fig. 7c). Conversely, SSA_t values span the 0.87–0.95 range without any significant dependence on η. Instantaneous SSA_t values of this study are in satisfactory accordance with those provided by Meloni et al. (2003). Lecce's g_t values are smaller than those retrieved at Lampedusa, where the contribution of coarse mode particles is on average larger, since Lampedusa is closer to the Africa coast.

ACPD
10, 20673–20727, 2010

The anthropogenic aerosol contribution is associated with a fraction f of the submicron size particles, in accordance with the discussion reported in Sect. 3b. The f value has been set equal to 0.73 and 0.80 for June and July, respectively, in accordance to Bergamo et al. (2008a). Then, MIE calculations are applied to translate the number concentration of anthropogenic particles into AOD_a, SSA_a, and g_a. Figure 8a shows the scatterplot of AOD_a/AOD_t ratios versus AOD_t. AOD_a/AOD_t ratios that are quite dependent on dusty-day vary from 0.27 up to 0.65 and allow inferring the role of anthropogenic particles in Mediterranean dust events. It is also worth noting from Fig. 8a that the contribution of anthropogenic particles decreases with AOD_t. Figure 8b and c show the scatterplot of SSA_a versus SSA_t and of g_a versus g_t, respectively. The comparison of Fig. 8 data to the ones reported by Bergamo et al. (2008a) allows inferring that AOD_a/AOD_t ratios, and SSA_a, and g_a values of this study are typical of Mediterranean costal sites.

5.3 Aerosol vertical distribution on dusty days

Lidar measurements at the closest time of AERONET measurements have been used to retrieve the aerosol vertical profile normalized to the AOD at 0.351 µm. The vertical profile of the AOD fraction is used in the aerosol radiative forcing calculations. Figure 9 shows the vertical profiles of all instantaneous dusty-day AOD fractions. The huge layer from about 5 to 8 km has been detected by the lidar on 24 July 2003. The grey line in Fig. 9 represents the mean vertical profile of the AOD fraction. Horizontal error bars represent ±1 standard deviation from the average value and indicate the AOD fraction variability. The high variability in time and space of the aerosol vertical distribution revealed by Fig. 9 is typical of Sahara dust intrusion events (e.g. Pavese et al., 2009). Aerosol particles up to 8 km have been monitored by the lidar during the analyzed dusty days.

ACPD
10, 20673–20727, 2010

5.4 Modeled solar, IR, and all-wave fluxes and comparisons

Figure 10a shows the scatterplot of the instantaneous solar (0.3–4.0 µm) fluxes at the surface calculated by the two-stream RTM versus the corresponding instantaneous surface fluxes (~0.3–2.8 µm) by AERONET. Different symbols are used to characterize different dusty days. Correlation coefficient ($r = 100\%$) and slope (0.998 ± 0.005) of the least-square fit reveal a very good accordance between our model and AERONET data, despite the different procedure used in the AERONET RTM to calculate the radiation field for a given distribution of aerosol optical properties. The root men square error (RMS = 7 Wm^{-2}) is also given in Fig. 10a. We believe that these results support the appropriateness of our model in the solar spectral range.

Modeled all-wave (solar+IR) fluxes at the surface are plotted in Fig. 10b as a function of surface all-wave-flux measurements performed at Lecce by an all-wave radiation transducer (p056 RADNT) which does not allow separating the solar and the IR component. All-wave-flux measurements are not available for 19 June 2006. The comparison show that instantaneous experimental and simulated all-wave fluxes are in satisfactory accordance: all-wave fluxes are highly correlated ($r = 97\%$) and the linear relation slope of modeled to observed fluxes is 1.1 ± 0.03 (least square slope). These last results also support the appropriateness of input data and of the used radiative transfer model. Modeled solar and IR fluxes at the surface, are plotted in Fig. 10c and d, respectively versus corresponding all-wave flux measurements to highlight their respective role at the surface and support the results of Fig. 10b. The regression line fitting the data points (dotted line) in addition to the 1:1 line (solid line) is plotted in Fig. 10c.

5.5 Instantaneous DREs by all particles on dusty days

Clear-sky, instantaneous DREs by all particles relating to the selected dusty-days (Table 2) are analyzed in this section. Figure 11a and b show ToA-DREs ($DRE_{t,ToA}$) at solar and IR wavelengths, respectively as a function of η (0.55 µm). sfc-DREs by all particles ($DRE_{t,sfc}$) versus η are plotted in Fig. 11d and e at solar and IR wavelengths,

ACPD
10, 20673–20727, 2010

respectively. Figure 11c and f show all-wave (solar+IR) DREs at the ToA and surface, respectively. We observe from Fig. 11a and d that $DRE_{t,ToA}$ and $DRE_{t,sfc}$ values at solar wavelengths span the – (38–11) m^{-2} and – (58–25) Wm^{-2} range, respectively and decrease in magnitude as η increases. The AOD_t increase for the larger contribution of coarse mode particles (Fig. 7a) as η decreases, contributes to these results. Hence, Sahara dust particles can exerts over south-eastern Italy quite large DREs, in accordance with previous studies (e.g., Haywood et al., 2003). It is noteworthy that ToA- and sfc-DRE values span within a wide range but, data points relating to a particular dusty-day vary within a smaller range. The strong dependence of aerosol optical and microphysical properties on dust event and more specifically on dust source and transport pathway, contribute to the high variability of the aerosol DRE (Fig. 11). The magnitude of the aerosol DRE at the surface is always larger than that at the ToA since aerosols not only scatter but, also absorb solar radiation. The solar $DRE_{t,sfc}/DRE_{t,ToA}$ ratio spans the 1.3–3.2 range in accordance with previous studies (e.g. Tafuro et al., 2007; Bergamo et al., 2008a–b; Meloni et al., 2003). Figure 11b and e show ToA- and sfc-DREs at IR wavelengths, respectively and reveal that both parameters on average decrease as η values increase, being the IR-DRE quite sensitive to the contribution of coarse mode particles mainly at the surface. IR-$DRE_{t,ToA}$ and IR-$DRE_{t,sfc}$ values vary up to 7 and 19 Wm^{-2} at the ToA and surface, respectively. In particular, the IR-$DRE_{t,ToA}$ offsets the solar-$DRE_{t,ToA}$ from 1% up to 26%. Whereas, the IR-$DRE_{t,sfc}$ offsets the solar-$DRE_{t,sfc}$ from 5% up to 47%. The largest offset percentage at the surface has been found on 17 July 2003. AOD_t and η reached the largest (0.71) and the smallest (0.34) value, respectively on this day (Fig. 7a). The largest offset percentage at the ToA has been found on 19 June 2006. Rather high and small AOD_t and η values, respectively have also been found on this day (Fig. 7a). These last results clearly show the importance of taking into account the IR-DRE mainly during dust intrusion events leading to $\eta < 0.5$.

Figure 12 shows the atmospheric forcing (AF_t) versus η. AF_t is defined as the difference between ToA and surface aerosol DRE at solar wavelengths. AF_t introduces part

ACPD
10, 20673–20727, 2010

of the remained in the atmosphere radiation and consequently may cause the heating effects. Thus, it is an indicator of aerosol effects on atmosphere dynamics. More specifically, AF_t leads to a stabilizing effect on the atmospheric stratification. Figure 12 reveals that AF_t values span the 8.8–35 Wm^{-2} range without any marked dependence on η.

Figure 13a–c show AOD_t (0.55 µm) and solar DREs at the ToA and surface versus the solar zenith angle (θ), in order to investigate the sensitivity of these parameters to θ. The results reported in this study are based on measurements performed at solar zenith angles spanning the 54°–76° range. AOD_t on average increases with θ (Fig. 13a). Its dependence on θ varies from day to day, since scattering and absorption processes depend on aerosol optical and microphysical properties, which may also vary with the time of the day. The dependence on θ of aerosol DREs also varies from day to day. However, on average, aerosol DREs reach a minimum values within the 60°-70° range at the ToA (Fig. 13b) and within the 55°–65° range at the surface (Fig. 13c). These results showing that the solar zenith angle contributes to the daily variability of instantaneous DREs at the ToA and surface, are in accordance with those reported by Meloni et al. (2005) and Derimian et al. (2008). The strong dependence of the upwelling radiation on the particle's dimensions for particles of large radii is responsible for the results of Fig. 13b–c.

Figure 14a–b shows the aerosol forcing efficiency (AFE) in the solar spectral range versus η at the ToA and surface, respectively. The AFE is defined as radiative effect per unit aerosol optical thickness and is mainly dependent on aerosol size and composition. In our study the AFE is calculated with respect to AOD_t at 0.55 µm. ToA- and sfc-AFE values span the – (81–45) Wm^{-2} and – (156–79) Wm^{-2} range, respectively and appear to not be significantly affected by η values. However, it is noteworthy that at the surface the radiative efficiency of aerosol with a large content of fine-mode particles can be even larger than that of less polluted dust aerosol. Solar-AFEs of this study are in satisfactory accordance with those recently provided by di Sarra et al. (2008) and Derimian et al. (2008). Di Sarra et al. (2008) found for desert dust particles, that

ACPD
10, 20673–20727, 2010

the surface shortwave AFE varied from −240 up to −100 Wm^{-2} for solar zenith angles varying within the 15–75° range. Ground based measurements of aerosol optical depth and shortwave irradiance at the Mediterranean island of Lampedusa were used by di Sarra et al. (2008) to calculate AFEs at the surface with respect to the optical depth at 496 nm. Instantaneous AFEs by Derimian et al. (2008) vary at the surface from −220 up to −30 Wm^{-2} and refer to dust aerosol and biomass-burning affected dust aerosol monitored over M'Bour (Senegal, Africa).

5.6 Instantaneous DREs by anthropogenic particles on dusty days

Results on the aerosol DRE by anthropogenic particles, calculated in accordance with the procedure outlined in Sect. 4.3 are analyzed in this section. Instantaneous solar-DREs by anthropogenic particles vary from −13 up to −7 Wm^{-2} and from −18 up to −11 Wm^{-2} at the ToA ($DRE_{a,ToA}$) and surface ($DRE_{a,sfc}$), respectively. Figure 15a and d show the scatterplot of $DRE_{a,ToA}/DRE_{t,ToA}$ and $DRE_{a,sfc}/DRE_{t,sfc}$ ratios versus η, respectively and reveal that the contribution of anthropogenic particles to DRE_t increases linearly with η both at the ToA and surface. The ToA-DRE by anthropogenic particles that represents on average 40% of that by all particles at $\eta \cong 0.4$, represents 80% of the $DRE_{t,ToA}$ at $\eta \cong 0.8$. 30% and 60% of the $DRE_{t,sfc}$ is due to anthropogenic particles at $\eta \cong 0.4$ and at $\eta \cong 0.8$, respectively. Hence, Fig. 15 clearly shows the significant contribution of anthropogenic particles to the Earth-Atmosphere energy balance during Mediterranean Sahara dust outbreaks. Several studies have revealed that η values spanning the 0.3–0.8 range are on average retrieved by satellite- and ground-based radiometer measurements, during Sahara dust intrusions over the Mediterranean (e.g. Santese et al., 2007; Meloni et al., 2007; Santese et al., 2008). Solid lines represent in Fig. 15a and d regression lines fitting the data points. Correlation coefficient (r) and slope (b) also are given in each plot. We believe that the high r values may lead assuming in the solar spectral range that:

$$DRE_{a,ToA} \cong \eta \times DRE_{t,ToA} \quad (3)$$

ACPD
10, 20673–20727, 2010

$$DRE_{a,sfc} \cong 0.7 \times \eta \times DRE_{t,sfc} \quad (4)$$

IR-DREs by anthropogenic particles span the 0.01–0.6 Wm^{-2} and the 0.3–1.7 Wm^{-2} range at the ToA and surface, respectively. The IR-$DRE_{a,ToA}$ offsets the solar-$DRE_{a,ToA}$ from 0.1% up to 4%. Whereas, the IR-$DRE_{a,sfc}$ offsets the solar-$DRE_{a,sfc}$ from 2% up to 11%. Figure 15b and e show the scatterplot of the IR-$DRE_{a,ToA}$/IR-$DRE_{t,ToA}$ and IR-$DRE_{a,sfc}$/IR-$DRE_{t,sfc}$ ratios versus η, respectively: the contribution of anthropogenic particles to IR-DRE_t increases linearly with η both at the ToA and surface. Solid lines represent regression lines fitting the data points. Hence, we can assume in the infrared spectral range, that:

$$\text{IR-}DRE_{a,ToA} \cong 0.2 \times \eta \times \text{IR-}DRE_{t,ToA} \quad (5)$$

$$\text{IR-}DRE_{a,sfc} \cong 0.3 \times \eta \times \text{IR-}DRE_{t,sfc} \quad (6)$$

Figure 15c and f show all-wave (solar+IR) DRE_a/DRE_t ratios versus η at the ToA and surface, respectively.

As a first approximation, valid at aerosol optical thicknesses sufficiently small that multiple aerosol scattering is a small fraction of aerosol extinction; DREs by natural and anthropogenic particles are linear in the amount of aerosol (Bates et al., 2006). Thus, in the limit of low aerosol optical depths, the linear assumption

$$DRE_t = DRE_a + DRE_n \quad (7)$$

is expected to hold, where DRE_n represents the DRE by natural particles. If we assume that the natural aerosol is mainly made by desert dust particles during Sahara dust intrusions, the aerosol DRE by dust (natural) particles can be estimated by the following relationships, in accordance with Eq. (7):

$$DRE_{n,ToA} \cong (1 - \eta) \times DRE_{t,ToA} \quad (8)$$

$$DRE_{n,sfc} \cong (1 - 0.7 \times \eta) \times DRE_{t,sfc} \quad (9)$$

ACPD
10, 20673–20727, 2010

$$\text{IR-DRE}_{n,\text{ToA}} \cong (1 - 0.2 \times \eta) \times \text{IR-DRE}_{t,\text{ToA}} \quad (10)$$

$$\text{IR-DRE}_{n,\text{sfc}} \cong (1 - 0.3 \times \eta) \times \text{IR-DRE}_{t,\text{sfc}} \quad (11)$$

A methodology to evaluate the DRE contribution by fine and coarse mode particles has been illustrated in this work. In particular, we believe that Eqs. (8–11) can be used to obtain a better estimate of the DRE by dust particles over the Mediterranean. The high η values that generally are found over Mediterranean and continental European sites affected by Sahara dust and the results on the chemical composition of ground collected particles during dust events, support the importance of taking into account the DRE by anthropogenic particles to properly estimate the DRE by dust particles over the Mediterranean basin and Europe.

However, uncertainties of size distributions must be low to properly account for the fine mode particle contribution and according to Kleidman et al. (2005). The AERONET inversion algorithm can overestimate the fine mode fraction mainly during strong dust events (η <0.6). Hence, if fine mode size distributions have been overestimated by AERONET during strong dust events, overestimated values of the DRE by anthropogenic particles are also provided by our model. More specifically, the study case analyzed in Sect. 4.4 has revealed that if the fine mode particle contribution is overestimated by 40%, anthropogenic aerosol DRE is also overestimated of about 40%. Size distribution measurements are needed to properly account for fine mode fractions but, these measurements that are usually performed at ground or by aircrafts to get size spectra at different altitudes from ground, can be quite expensive and are available only for rather few study cases. As a consequence, synthetic or AERONET size distributions are usually used in radiative transfer calculations (e.g. Derimian et al., 2008). AERONET products are extensively used as the only ground truth in aerosol-related research.

ACPD
10, 20673–20727, 2010

6 Summary and conclusion

Nine Sahara dust outbreaks that have affected the Mediterranean basin and south-east Italy from 2003 to 2006 have been selected to calculate clear-sky instantaneous DREs by all and anthropogenic particles.

Aerosol optical and microphysical properties have firstly been analyzed to contribute to the characterization of the mean optical properties of the Mediterranean aerosol affected by the intrusion of Sahara dust particles. We have found that aerosol properties are quite dependent on dusty day. Soil properties of source regions, transport pathways and anthropogenic particles contribute to the observed high variability of aerosol properties. Instantaneous n and k values at 0.44 µm span the 1.33–1.55 and 0.0037–0.014 range, respectively during the analyzed dust outbreaks and fine mode particles contribute from 34% to 85% to the total AOD. The variability range of n and k values and the contribution of anthropogenic particles decrease as the AOD increases. In particular, we have found that at AODs (0.44 µm) >0.45, the contribution of fine mode particles becomes smaller than 55% and the columnar averaged value ±1 SD of n and k is: $< n > = 1.48 \pm 0.01$ and $< k > = 0.007 \pm 0.002$, in accordance with previous studies (Tafuro et al., 2006).

The aerosol DRE has been calculated in the solar (0.3–4 µm) and infrared (4–200 µm) spectral range, at the top of the atmosphere (ToA) and at the Earth's surface (sfc). Observation-based meteorological and aerosol parameters have been used to initialize the two-stream radiative transfer model. The appropriateness of input and output model data has been demonstrated by the comparison of simulated surface all-wave fluxes to broadband all-wave flux measurements at the surface and in the solar spectral range, by the comparison with modelled surface fluxes by AERONET.

Instantaneous DREs, in addition to the AF and AFEs have been calculated to investigate aerosol radiative effects during dust events. We have found that the instantaneous solar-DRE by all particles (DRE_t) spans the – (38–11) Wm^{-2} and the – (58–25) Wm^{-2} range at the ToA and surface, respectively as a consequence of the high variability of

ACPD
10, 20673–20727, 2010

aerosol optical and microphysical properties. We have also observed that the solar zenith angle is mainly responsible for the daily variability of the aerosol DRE. The IR-$DRE_{t,sfc}$ by all particles offsets the solar-$DRE_{t,sfc}$ from 5% up to 47%. Whereas, the IR-$DRE_{t,ToA}$ offsets the solar-$DRE_{t,ToA}$ from 1% up to 26%. Hence, the importance of taking into account the aerosol IR-DRE during dust intrusion events has been demonstrated.

DREs by anthropogenic particles have also been evaluated. The anthropogenic aerosol contribution has been associated with a fraction f of the number concentration of fine-mode aerosol $N_f(r)$ provided by AERONET, in accordance to Bergamo et al. (2008a). Then, we have found that the AOD at 0.55 µm by anthropogenic particles represents from 27% up to 65% of the AOD_t. This result highlights the role of anthropogenic particles in Mediterranean dust events, if we assume that AERONET size distributions are accurate. DREs by natural and anthropogenic particles have been considered linear in the amount of aerosol present, as a first approximation. Then, a linear relationship dependent on the fine mode fraction η and on the total aerosol DRE has been retrieved to calculate the DRE by natural and anthropogenic particles in the solar and infrared spectral range. In particular, by assuming that all natural particles are from the Sahara deserts, we have found that the instantaneous solar-DRE by desert particles represents from 20% up to 65% and from 45% up to 76% of the instantaneous solar-DRE by all particles at the ToA and surface, respectively. The instantaneous IR-DRE by desert particles represents from 84% up to 93% and from 76% up to 90% of the instantaneous IR-DRE by all particles at the ToA and surface, respectively. We believe that our results highlight for the first time, to the best of our knowledge, the role of anthropogenic particles (mainly in the solar spectral range), during dust intrusions events in the Mediterranean basin. The significant presence of anthropogenic particles during dust events has also been revealed by chemical analyses on ground collected particles (e.g. Bellantone et al., 2008; Carofalo et al., 2008). Hence, the methodology used in the paper should allow getting more reliable estimates of the DRE by desert dust particles over Europe.

ACPD
10, 20673–20727, 2010

The dependence of our results on the accuracy of volume size distributions retrieved by the AERONET inversion algorithm represents the main weak point of the paper. Kleidman et al. (2005) have shown that the Dubovik inversion of sky radiances can overestimate fine fractions for dust aerosol by 0.1–0.2 relative to the O'Neill method of inverting AERONET AOD spectra. In particular, they have shown that fine-mode-fraction overestimations become significant at $\eta < 0.6$. Then, according to Kleidman et al. (2005), DREs by anthropogenic and coarse mode particles have probably been over- and under-estimated, respectively, during strong dust outbreaks (η <0.6). Work is in progress to investigate the accuracy of size distributions retrieved by AERONET during strong dust events by performing size spectra measurements at ground.

Aerosol properties from sun/sky radiometer measurements performed at Lecce (a peninsular site in south-east Italy) during selected dust outbreaks have been used in this study. Nevertheless, we believe that paper's results can be representative of several Mediterranean sites, in accordance to Bergamo et al. (2008a) and hence, contribute to the characterization of aerosol effects on the energy-balance of the Mediterranean: one of the most responsive regions to climate change. Last but not least, the used methodology can generally be applied to evaluate the DRE contribution by fine and coarse mode particles.

Acknowledgements. This work is supported by "Progetto Strategico SIMPA" financed by Regione Puglia (Italy), by the European Project EARLINET-ASOS (2006–2011, contract n. 025991), and by Progetto FISR AEROCLOUDS. The authors kindly acknowledge Stefan Kinne for providing the two-stream radiative transfer model and for the constructive discussions.

References

Balkanski, Y., Schulz, M., Claquin, T., and Guibert, S.: Reevaluation of Mineral aerosol radiative forcings suggests a better agreement with satellite and AERONET data, Atmos. Chem. Phys., 7, 81–95, doi:10.5194/acp-7-81-2007, 2007.

Bates, T. S., Anderson, T. L., Baynard, T., Bond, T., Boucher, O., Carmichael, G., Clarke, A.,

ACPD

10, 20673–20727, 2010

Erlick, C., Guo, H., Horowitz, L., Howell, S., Kulkarni, S., Maring, H., McComiskey, A., Middlebrook, A., Noone, K., O'Dowd, C. D., Ogren, J., Penner, J., Quinn, P. K., Ravishankara, A. R., Savoie, D. L., Schwartz, S. E., Shinozuka, Y., Tang, Y., Weber, R. J., and Wu, Y.: Aerosol direct radiative effects over the northwest Atlantic, northwest Pacific, and North Indian Oceans: estimates based on in-situ chemical and optical measurements and chemical transport modeling, Atmos. Chem. Phys., 6, 1657–1732, doi:10.5194/acp-6-1657-2006, 2006.

Bellantone, V., Carofalo, I., De Tomasi, F., Perrone, M. R., Santese, M., Tafuro, A. M., and Turnone, A.: In situ samplings and remote sensing measurements to characterize aerosol properties over South-East Italy, J. Atmos. Ocean. Tech., 25(8), 1341–1356, 2008.

Bergamo, A., Tafuro, A. M., Kinne, S., De Tomasi, F., and Perrone, M. R.: Monthly-averaged anthropogenic aerosol direct radiative forcing over the Mediterranean based on AERONET aerosol properties, Atmos. Chem. Phys., 8, 6995–7014, doi:10.5194/acp-8-6995-2008, 2008a.

Bergamo, A., De Tomasi, F., and Perrone, M. R.: Direct radiative effects by anthropogenic particles at a polluted site: Rome (Italy), Il Nuovo Cimento, 31C, 513–526, doi:10.1393/ncc/i2009-10320-1, 2008b.

Carofalo I., Fermo, P., Perrone, M. R., and Piazzalunga, A.: Advection patterns and composition of TSP and PM2.5 samples over south-east Italy, Proceeding in: Chemical Engineering Transactions, 18, 185–192, 2008.

Dahlback, A. and Stamnes, K.: A new spherical model for computing the radiation field available for photolysis and heating at twilight, Planetary and Space Science (ISSN 0032-0633), 39, 671–683, doi:10.1016/0032-0633(91)90061-E, 1991.

Dentener, F., Kinne, S., Bond, T., Boucher, O., Cofala, J., Generoso, S., Ginoux, P., Gong, S., Hoelzemann, J. J., Ito, A., Marelli, L., Penner, J. E., Putaud, J.-P., Textor, C., Schulz, M., van der Werf, G. R., and Wilson, J.: Emissions of primary aerosol and precursor gases in the years 2000 and 1750 prescribed data-sets for AeroCom, Atmos. Chem. Phys., 6, 4321–4344, doi:10.5194/acp-6-4321-2006, 2006.

Derimian, Y., Leon, J.-F., Dubovik, O., Chiapello, I., Tanré, D., Sinyuk, A., Auriol, F., Podvin, T., Brogniez, G., and Holben, B. N.: Radiative properites of aerosol mixture observed during the dry season 2006 over M'Bour, Senegal (African Monsoon Multidisciplinary Analysis campaign), J. Geophys. Res, 113, D00C09, doi:10.1029/2008JD009904, 2008.

De Tomasi, F., Blanco, A., and Perrone, M. R.: Raman lidar monitoring of extinction and backscattering of Africa dust layers and dust characterization, Appl. Optics, 42, 1699–1709,

ACPD
10, 20673–20727, 2010

2003.
De Tomasi, F., Tafuro, A. M., and Perrone, M. R: Height and seasonal dependence of aerosol optical properties over south-east Italy, J. Geophys. Res., 111, D10203, doi:10.1029/2005JD006779, 2006.
di Sarra, A., Di Iorio, T., Cacciani, M., Fiocco, G., and Fua', D.: Saharan dust profiles measured by lidar at Lampedusa, J. Geophys. Res., 106, 10335–10347, 2001.
di Sarra, A., Pace, G., Meloni, D., De Silvestri, L., Piacentino, S., and Monteleone, F.: Surface shortwave radiative forcing of different aerosol types in the central Mediterranean, Geophys. Res. Lett., 35L02714, doi:10.1029/2007GL032395, 2008.
Dubovik, O., Holben, B. N., Lapyonok, T., Sinyk, A., Mishechenko, M. I., Yang, P., and Slutsker, I.: Non-spherical aerosol retrieval method employing light scattering by spheroids, J. Geophys. Res. Lett., 29, 54-1–54-4, 2002.
Dubovik, O., Sinyuk, A., Lapyonok, T., Holben, B. N., Mishchenko, M., Yang, P., Eck, T. F., Volten, H., Muñoz, O., Veihelmann, B., Van Der Zande, W. J., Leon, J. F., Sorokin, M., and Slutsker, I.: Application of spheroid models to account for aerosol particle nonsphericity in remote sensing of desert dust, J. Geophys. Res., 111, D11208, doi:10.1029/2005JD006619, 2006.
Dubuisson, P., Buriez, J. C., and Fouquart, Y.: High spectral resolution solar radiative transfer in absorbing and scattering media, application to the satellite simulation, J. Quant. Spectrosc. Radiat. Transfer, 55(1), 103–126, 1996.
Fotiadi, A., Hatzianastassiou, N., Drakakis, E., Matsoukas, C., Pavlakis, K. G., Hatzidimitriou, D., Gerasopoulos, E., Mihalopoulos, N., and Vardavas, I.: Aerosol physical and optical properties in the Eastern Mediterranean Basin, Crete, from Aerosol Robotic Network data, Atmos. Chem. Phys., 6, 5399–5413, doi:10.5194/acp-6-5399-2006, 2006.
García, O. E., Díaz, A. M., Exposito, F. J., Dýaz, J. P., Dubovik, O., Dubuisson, P., Roger, J.-C., Eck, T. F., Sinyuk, A., Derimian, Y., Dutton, E. G., Schafer, J. S., Holben, B. N., and García, C. A.: Validation of AERONET estimates of atmospheric solar fluxes and aerosol radiative forcing by ground-based broadband measurements, J. Geophys. Res., 113, D21207, doi:10.1029/2008JD010211, 2008.
Haywood, J., Francis, P., Osborne, S., Glew, M., Loeb, N., Highwood, E., Tanré, D., Myhre, D., Formenti, P., and Hirst, E.: Radiative properties and direct radiative effect of Saharan dust measured by the C-130 aircraft during SHADE: 1. Solar spectrum, J. Geophys. Res., 108(D18), 8577, doi:10.1029/2002JD002687, 2003.

ACPD
10, 20673–20727, 2010

Hamonou, E., Chazette, P., Balis, D., Dulac, F., Scheider, X., Galani, E., Ancellet, G., and Papayannos, A.: Characterization of the vertical structure of Saharan dust export to the Mediterranean basin, J. Geophys. Res., 104, 22257–22270, 1999.

Hatzianastassiou, N., Matsoukas, C., Fotiadi, A., P. W. Stackhouse Jr., Koepke, P., Pavlakis, K. G., and Vardavas, I.: Modelling the direct effect of aerosols in the solar near-infrared on a planetary scale, Atmos. Chem. Phys., 7, 3211–3229, doi:10.5194/acp-7-3211-2007, 2007.

Holben, B. N., Eck, T. F., Slutsker, I., Tanré, D., Buis, J. P., Setzer, A., Vermote, E., Reagan, J. A., Kaufman, Y. J., Nakajima, T., Lavenu, F., Jankowiak, I., and Smirnov, A.: AERONET – a federate instrument network and data archive for aerosol characterization, Remote Sens. Environ., 66, 1–16, 1998.

Kay, M. J., Box, M. A., Trautmann, T., and Landgraf, J.: Actinic flux and net flux calculations in radiative transfer-A comparative study of computational efficiency, J. Atmos. Sci., 58, 3752–3761, 2001.

King, M. D., Kaufman, Y. J., Menzel, W. P., Tanré, D.: Remote Sensing of Cloud, Aerosol, and Water Vapor Properties from the Moderate Resolution Imaging Spectrometer (MODIS), IEEE T. Geosci. Remote, 30, 1–27, 1992.

Kleidman, R. G., O'Neill, N. T, Remer, L. A., Kaufman, Y. J., Eck, T. F., Didier Tanre', D., Dubovik, O., and Holben, B. N: Comparison of Moderate Resolution Imaging Spectroradiometer (MODIS) and Aerosol Robotic Network (AERONET) remote-sensing retrievals of aerosol fine mode fraction over ocean, J. Geophys. Res., 110, D22205, doi:10.1029/2005JD005760, 2005.

Mallet, M., Tulet, P., Serça, D., Solmon, F., Dubovik, O., Pelon, J., Pont, V., and Thouron, O.: Impact of dust aerosols on the radiative budget, surface heat fluxes, heating rate profiles and convective activity over West Africa during March 2006, Atmos. Chem. Phys., 9, 7143–7160, doi:10.5194/acp-9-7143-2009, 2009.

Matthias, V., Balis, D., Boesenberg, J., Eixmann, R., Iarlori, M., Komguem, L., Mattis, I., Papayannis, A., Pappalardo, G., Perrone, M. R.,and Wang, X.: Vertical aerosol distribution over Europe: Statistical analysis of Raman lidar data from 10 European Aerosol Research Lidar Network (EARLINET) stations, J. Geophys. Res., 109, D18201, doi:10.1029/2004JD004638, 2004.

Mayer, B., Seckmeyer, G., and Kylling, A.: Systematic long-term comparison of spectral UV measurements and UVSPEC modeling results, J. Geophys. Res., 102, 8755–8767, 1997.

Mayer, B. and Kylling, A.: Technical note: The libRadtran software package for radiative trans-

ACPD

10, 20673–20727, 2010

fer calculations – description and examples of use, Atmos. Chem. Phys., 5, 1855–1877, doi:10.5194/acp-5-1855-2005, 2005.
Meador, W. E and Weaver, W. R.: Two-stream approximation to radiative transfer in planetary atmospheres: a unified description of existing methods and new improvement, J. Atmos. Sci., 37, 630–643, 1980.
Meloni, D., di Sarra, A., Di Iorio, T., Fiocco, G., Junkermann, W., and Pace, G.: Tropospheric aerosols in the Mediterranean: 2. Radiative effects through model simulations and measurements, J. Geophys. Res., 108(D10), 4317, doi:10.1029/2002JD002807, 2003.
Meloni, D., di Sarra, A., Di Iorio, T., and Fiocco G.: Direct radiative forcing of sahara dust in the mediterranean from measurements at Lampedusa Island and MISR space-borne observations, J. Geophys. Res., 109, D08206, doi:10.1029/2003JD003960, 2004.
Meloni, D., di Sarra, A., Di Iorio, T., and Fiocco, G.: Influence of the vertical profile of Saharan dust on the visible direct radiative forcing, J. Quant. Spectrosc. Ra., 93, 347–413, 2005.
Meloni, D., di Sarra, A., Biavati, G., DeLuisi, J. J., Monteleone F., Pace, G., Piacentino, S., and Sferlazzo, D. M.: Seasonal behavior of Saharan dust events at the Mediterranean island of Lampedusa in the period 1999–2005, Atmos. Environ., 41, 3041–3056, 2007.
Mishchenko, M. I., Travis, L. D., Kahn, R. A., and West, R. A.: Modeling phase functions for dustlike tropospheric aerosols using a shape mixture of randomly oriented polydisperse spheroids, J. Geophys. Res, 102, 16831–16847, 1997.
Papayannis, A., Amiridis, V., Mona, L., Tsaknakis, G., Balis, D., Bösenberg, J., Chaikovski, A., De Tomasi, F., Grigorov, I., Mattis, I., Mitev, V., Müller, D., Nickovic, S., Pérez, C., Pietruczuk, A., Pisani, G., Ravetta, F., Rizi, V., Sicard, M., Trickl, T., Wiegner, M., Gerding, M., Mamouri, R. E., D'Amico, G., and Pappalardo G.: Systematic lidar observations of Saharan dust over Europe in the frame of EARLINET (2000–2002), J. Geophys. Res, 113, D10204, doi:10.1029/2007JD009028, 2008.
Pavese, G., De Tomasi, F., Calvello, M., Esposito, F., and, Perrone, M. R.: Detection of Sahara dust intrusions during mixed advection patterns over south-east Italy: a case study, Atmos. Res., 92, 489–504, doi:10.1016/j.atmosres.2009.02.003, 2009.
Perez, C., Nickovic, S., Baldasano, J. M., Sicard, M., rocadenbosch, F., and Cachorro, V. E.: A long Saharan dust event over the western Mediterranean: lidar, Sun photometer observations, and regional dust modeling, J. Geophys. Res., 111, D15214, doi:10.1029/2005JD006579, 2006.
Raut, J.-C. and Chazette, P.: Radiative budget in the presence of multi-layered aerosol

ACPD
10, 20673–20727, 2010

structures in the framework of AMMA SOP-0, Atmos. Chem. Phys., 8, 6839–6864, doi:10.5194/acp-8-6839-2008, 2008.
Reddy, M. S., Boucher, O., Balanski, Y., and Schulz, M.: Aerosol optical depths and direct radiative perturbations by species and source type, Geophys. Res. Lett., 32, L12803, doi:10.1029/2004GL021743, 2005.
Santese, M., De Tomasi, F., and Perrone, M. R.: Moderate Resolution Imaging Spectroradiometer (MODIS) and Aerosol Robotic Network (AERONET) retrievals during dust outbreaks over the Mediterranean, J. Geophys. Res., 112, D18201, doi:10.1029/2007JD008482, 2007.
Santese, M., De Tomasi, F., and Perrone, M. R.: Advection patterns and aerosol optical and microphysical properties by AERONET over south-east Italy in the central Mediterranean, Atmos. Chem. Phys., 8, 1881–1896, doi:10.5194/acp-8-1881-2008, 2008.
Schulz, M., Textor, C., Kinne, S., Balkanski, Y., Bauer, S., Berntsen, T., Berglen, T., Boucher, O., Dentener, F., Guibert, S., Isaksen, I. S. A., Iversen, T., Koch, D., Kirkevåg, A., Liu, X., Montanaro, V., Myhre, G., Penner, J. E., Pitari, G., Reddy, S., Seland, Ø., Stier, P., and Takemura, T.: Radiative forcing by aerosols as derived from the AeroCom present-day and pre-industrial simulations, Atmos. Chem. Phys., 6, 5225–5246, doi:10.5194/acp-6-5225-2006, 2006.
Sokolik, I. N., Winker, D., Bergametti, G., Gillette, D., Carmichael, G., Kaufman, Y., Gomes, L., Schuetz, L., and Penner J.: Introduction to special section on mineral dust: outstanding problems in quantifying the radiative impact of mineral dust, J. Geophys. Res., 106, 18015–18027, 2001.
Stamnes, K., Tsay, S., Wiscombe, W., and Jayaweera, K.: A numerically stable algorithm for discrete-ordinate-method radiative transfer in multiple scattering and emitting layered media, Appl. Opt., 27, 2502–2509, 1988.
Stier, P., Seinfeld, J. H., Kinne, S., and Boucher, O.: Aerosol absorption and radiative forcing, Atmos. Chem. Phys., 7, 5237–5261, doi:10.5194/acp-7-5237-2007, 2007.
Tafuro, A. M., Banaba, F., De Tomasi, F., Perrone, M. R., and Gobbi, G. P.: Saharan dust particle properties over the central Mediterranean, Atmos. Res., 81, 67–93, 2006.
Tafuro, A. M., Kinne, S., De Tomasi, F., and Perrone, M. R.: Annual cycle of aerosol direct radiative effect over southeast Italy and sensitivity studies, J. Geophys. Res., 112, D20202, doi:10.1029/2006JD008265, 2007.
Tafuro, A. M., De Tomasi, F., and Perrone, M. R.: Remote Sensing of Aerosols by Sunphotometers and Lidar Techniques, Chapter 14, in: Advanced Environmental Monitoring, edited by: Kim, Y. J., Platt, U., Springer, ISBN 978-1-4020-6363-3, XXII, 179–189, 2008.

ACPD
10, 20673–20727, 2010

Tegen, I.: Modeling the mineral dust aerosol cycle in the climate system, Quant. Sci. Rev., 22, 1821–1834, 2003.

Yu, H., Kaufman, Y. J., Chin, M., Feingold, G., Remer, L. A., Anderson, T. L., Balkanski, Y., Bellouin, N., Boucher, O., Christopher, S., DeCola, P., Kahn, R., Koch, D., Loeb, N., Reddy, M. S., Schulz, M., Takemura, T., and Zhou, M.: A review of measurement-based assessments of the aerosol direct radiative effect and forcing, Atmos. Chem. Phys., 6, 613–666, doi:10.5194/acp-6-613-2006, 2006.

Zhou, Mi, Yu, H., Dickinson, R. E., Dubovik, O., and Holben, B. N.: A normalized description of the direct effect of key aerosol types on solar radiation as estimated from Aerosol Robotic Network aerosols and Moderate Resolution Imagining Spectroradiometer albedos, J. Geophys. Res., 110, D19202, doi:10.1029/2005JD005909, 2005.

ACPD

10, 20673–20727, 2010

Table 1. Real (n) and imaginary (k) refractive index at IR subbands.

λ (μm)	n	k
4.250E+00	1.490	480E-02
5.350E+00	1.500	270E-01
6.250E+00	1.420	460E-01
7.350E+00	1.440	660E-01
8.750E+00	1.380	400E+00
1.030E+01	2.050	560E+00
1.175E+01	1.790	200E+00
1.390E+01	1.640	210E+00
1.720E+01	1.520	390E+00
2.430E+01	3.060	840E+00
3.700E+01	2.400	650E+00
8.000E+01	2.200	700E+00

ACPD
10, 20673–20727, 2010

Table 2. Instantaneous values of AOD, real (n) and imaginary (k) refractive index at 0.44 µm, of the Angstrom coefficient (Å) computed from AOD values at 0.44 µm and 0.87 µm, of the sphericity parameter (S), and surface albedo values (α) retrieved from AERONET sun/sky radiometer measurements during the selected dusty days observed at Lecce from 2003 to 2006.

dd month yyyy	hh:mm	AOD (0.44 µm)	Å	S %	n (0.44 µm)	k (0.44 µm)	α (0.3–0.7 µm)	α (0.7–5 µm)
17 July 2003	04:59	0.71	0.23	1.4	1.47	0.0044	0.11	0.37
24 July 2003	06:58	0.44	0.63	0.3	1.42	0.0055	0.097	0.31
24 July 2003	14:52	0.38	0.65	1.1	1.41	0.0056	0.098	0.31
24 July 2003	15:24	0.41	0.69	0.8	1.42	0.0070	0.10	0.32
24 July 2003	16:26	0.41	0.66	5.9	1.44	0.0079	0.11	0.38
8 July 2004	14:59	0.34	0.70	1.6	1.47	0.0059	0.097	0.31
8 July 2004	15:29	0.33	0.68	1.0	1.44	0.0059	0.10	0.32
8 July 2004	16:25	0.32	0.68	2.8	1.49	0.0050	0.11	0.36
5 July 2005	14:58	0.25	1.38	19.9	1.52	0.0096	0.10	0.31
5 July 2005	15:30	0.27	1.35	19.7	1.50	0.014	0.10	0.32
5 July 2005	16:26	0.31	1.51	31.8	1.52	0.011	0.11	0.36
5 July 2005	16:54	0.32	1.50	40.4	1.53	0.011	0.11	0.38
6 July 2005	14:59	0.28	1.06	16.1	1.50	0.0054	0.10	0.31
6 July 2005	15:30	0.32	1.09	12.6	1.55	0.0037	0.10	0.32
6 July 2005	16:26	0.35	1.25	8.7	1.46	0.0039	0.11	0.36
6 July 2005	16:53	0.34	1.36	25.1	1.33	0.0054	0.11	0.38
18 July 2005	15:00	0.32	0.87	29.1	1.44	0.0095	0.10	0.31
18 July 2005	15:27	0.42	0.84	44.1	1.48	0.011	0.10	0.32
18 July 2005	16:49	0.40	0.90	8.0	1.52	0.0093	0.11	0.38
19 June 2006	15:30	0.49	0.34	1.8	1.49	0.0074	0.09	0.31
19 June 2006	16:26	0.52	0.36	1.7	1.47	0.0066	0.10	0.34
19 June 2006	16:53	0.53	0.38	2.2	1.47	0.0083	0.10	0.37
22 June 2006	15:31	0.39	0.46	1.5	1.50	0.0097	0.093	0.31
22 June 2006	16:27	0.42	0.52	1.9	1.43	0.0082	0.10	0.34
26 June 2006	15:00	0.32	0.76	27.5	1.44	0.0075	0.097	0.31
26 June 2006	15:31	0.34	0.61	46.6	1.45	0.0075	0.10	0.32

ACPD
10, 20673–20727, 2010

Table 3. Instantaneous AOD, SSA, and *g* values at 0.55 µm by MIE calculations and AERONET products for 22 June 2006 at different day hours. AERONET AOD, SSA, and *g* values at 0.44 and 0.675 µm, respectively have been averaged to calculate AOD, SSA, and *g* values at 0.55 µm.

	Mie code			AERONET		
Time (UTC)	AOD	SSA	*g*	AOD	SSA	G
15:31	0.34	0.87	0.66	0.35	0.89	0.71
16:27	0.37	0.90	0.66	0.38	0.91	0.70

ACPD
10, 20673–20727, 2010

Table 4. Instantaneous surface net-flux (F_{sfc}) in the solar (0.3–4 µm) and IR (4–200 µm) spectral range, AOD at 0.55 µm by fine (AOD_f) and anthropogenic (AOD_a) particles, DRE by all (DRE_t) and anthropogenic (DRE_a) particles at the top of the atmosphere (ToA) and surface (sfc), in the solar (0.3–4 µm) and IR (4–200 µm) spectral range for 22 June 2006 at different day hours. Corrected AOD (AOD_{cor}) and DRE (DRE_{cor}) values calculated in accordance with Eq. (2) are also reported.

Parameter	(0.3–4) µm		(4–200) µm	
Time (UTC)	15:31	16:27	15:31	16:27
F_{sfc} (Wm^{-2})	331	184	−72	−71
$DRE_{t,ToA}$ (Wm^{-2})	−20	−25	1.7	1.8
$DRE_{t,sfc}$ (Wm^{-2})	−53	−45	9.1	10.0
AOD_f (0.55 µm)	0.16	0.17		
AOD_a (0.55 µm)	0.12	0.13		
$DRE_{a,ToA}$ (Wm^{-2})	−9.6	−11	0.03	0.04
$DRE_{a,sfc}$ (Wm^{-2})	−15	−15	0.92	1.3
$AOD_{f,cor}$ (0.55 µm)	0.10	0.10		
$AOD_{a,cor}$ (0.55 µm)	0.06	0.07		
$DRE_{a,cor,ToA}$ (Wm^{-2})	−5.5	−6.3	0.02	0.02
$DRE_{a,cor,sfc}$ (Wm^{-2})	−8.3	−8.5	0.51	0.71

ACPD
10, 20673–20727, 2010

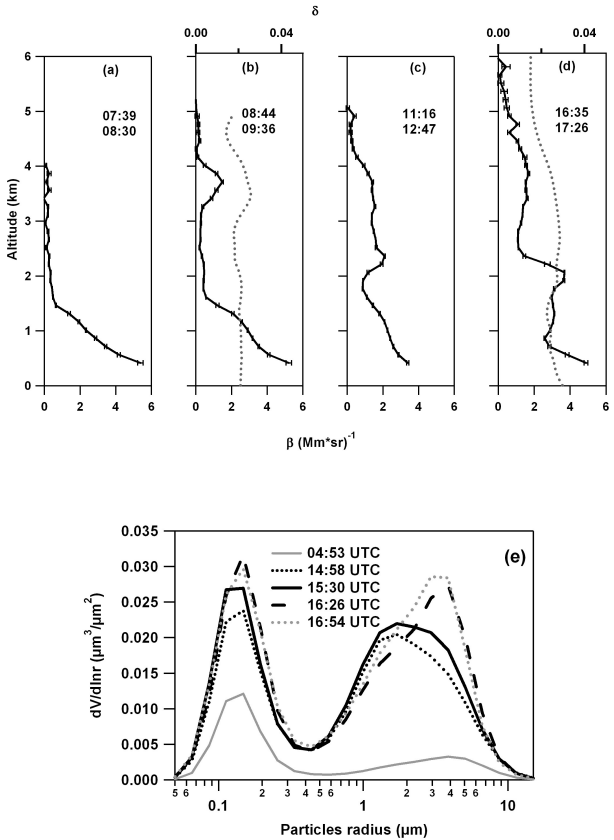

Fig. 1. (a–d) Aerosol backscatter coefficient profiles (solid lines) from lidar measurements performed on 5 July 2005 at different day hours (UTC). Grey dotted lines represent vertical profiles of the depolarization ratio. **(e)** Columnar volume size distributions from AERONET sun/sky photometer measurements performed on 5 July 2005 at different day hours.

ACPD
10, 20673–20727, 2010

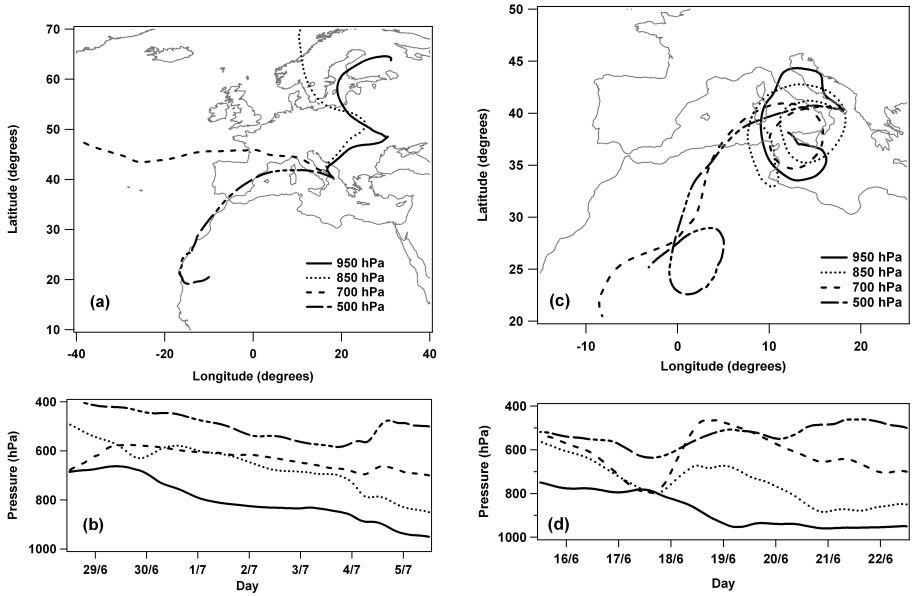

Fig. 2. Pathways of the 7-day analytical back trajectories at 950, 850, 700, and 500 hPa reaching Lecce at 12:00 UTC **(a)** on 5 July 2005 and **(c)** on 22 June 2006. Altitude of each back trajectory as a function of time **(b)** on 5 July 2005 and **(d)** on 22 June 2006.

ACPD
10, 20673–20727, 2010

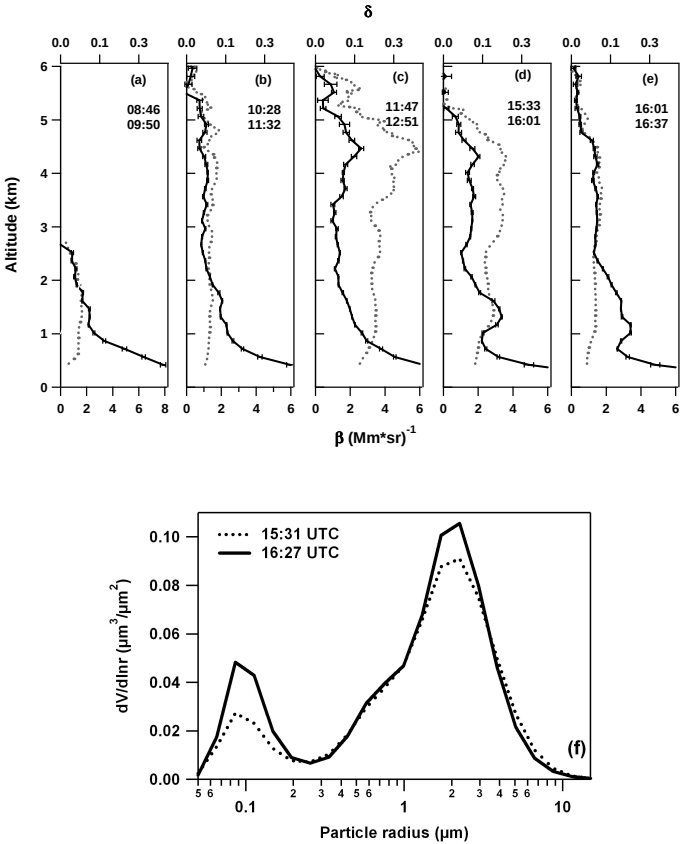

Fig. 3. **(a–e)** Aerosol backscatter coefficient profiles (solid lines) from lidar measurements performed on 22 June 2006 at different day hours (UTC). Grey dotted lines represent vertical profiles of the depolarization ratio. **(f)** Columnar volume size distributions from AERONET sun/sky photometer measurements performed on 22 June 2006 at 15:31 (dotted line) and at 16:27 UTC (solid line).

ACPD
10, 20673–20727, 2010

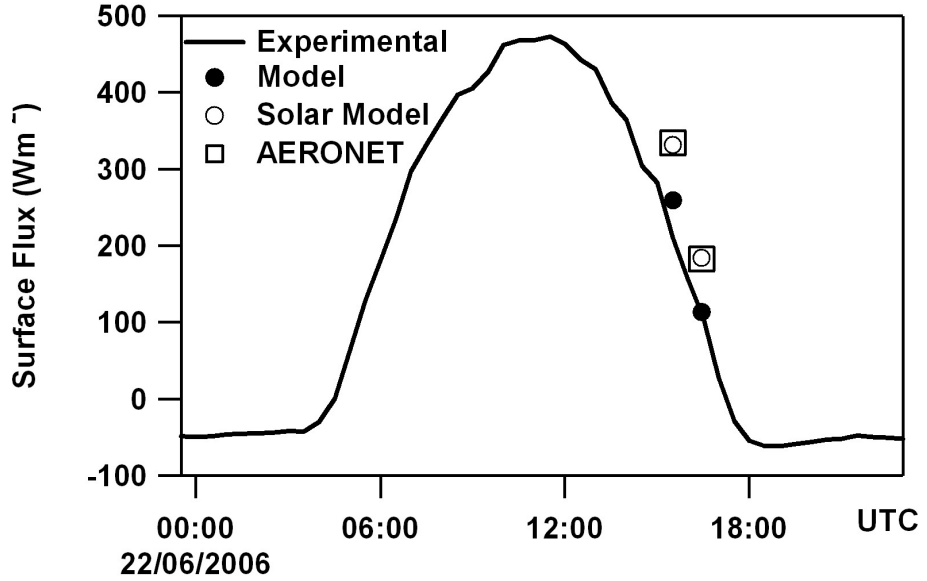

Fig. 4. Broadband (0.3–30 µm) flux measurements at the surface (solid line) by a net radiation transducer. Full dots represent modeled instantaneous all-wave fluxes at the surface. Open dots and open boxes represent solar fluxes at the surface by the model and by AERONET, respectively.

ACPD
10, 20673–20727, 2010

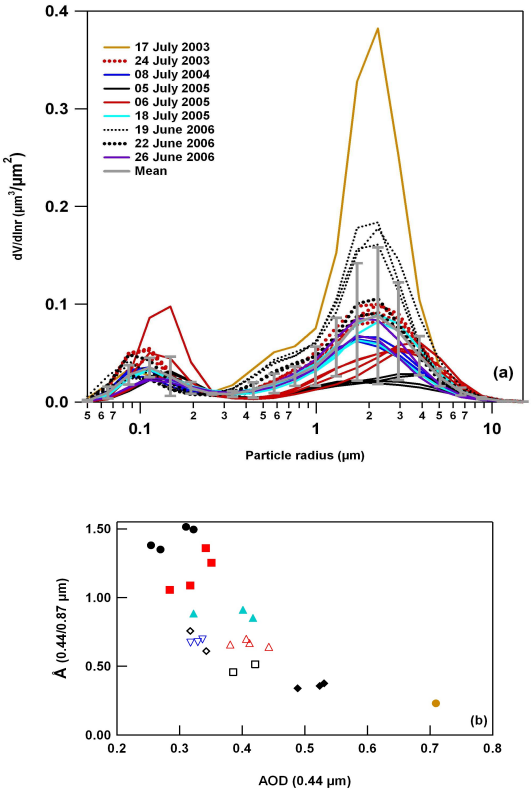

Fig. 5. (a) Instantaneous columnar volume size distributions of the selected dusty days. The grey line represents the mean columnar volume size distribution. Vertical bars represent ±1 standard deviation from the average value. **(b)** Instantaneous Angstrom coefficient values computed from AODs at 0.44 μm and 0.87 μm versus the AOD at 0.44 μm. Different symbols are used to characterize different dusty-days: 17 July 2003 (●); 24 July 2003 (△); 8 July 2004 (▽); 5 July 2005 (●); 6 July 2005 (■); 18 July 2005 (▲); 19 June 2006 (◆); 22 June 2006 (□); 26 June 2006 (◇).

ACPD
10, 20673–20727, 2010

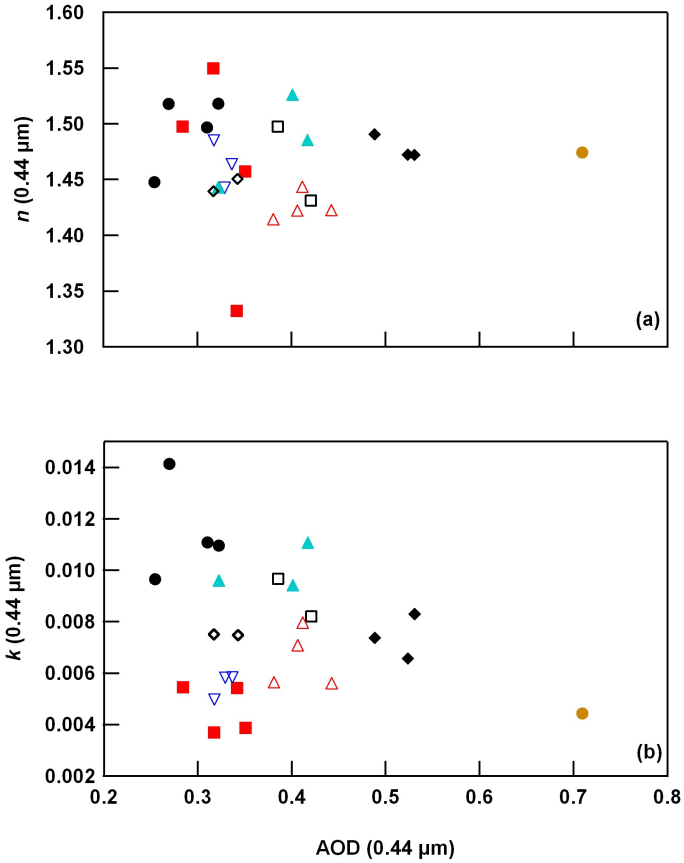

Fig. 6. Instantaneous values at 0.44 µm of **(a)** *n* and **(b)** *k* versus the AOD by all particles. Different symbols are used to characterize different dusty-days: 17 July 2003 (●); 24 July 2003 (△); 8 July 2004 (▽); 5 July 2005 (⬟); 6 July 2005 (■); 18 July 2005 (▲); 19 June 2006 (◆); 22 June 2006 (□); 26 June 2006 (◇).

ACPD
10, 20673–20727, 2010

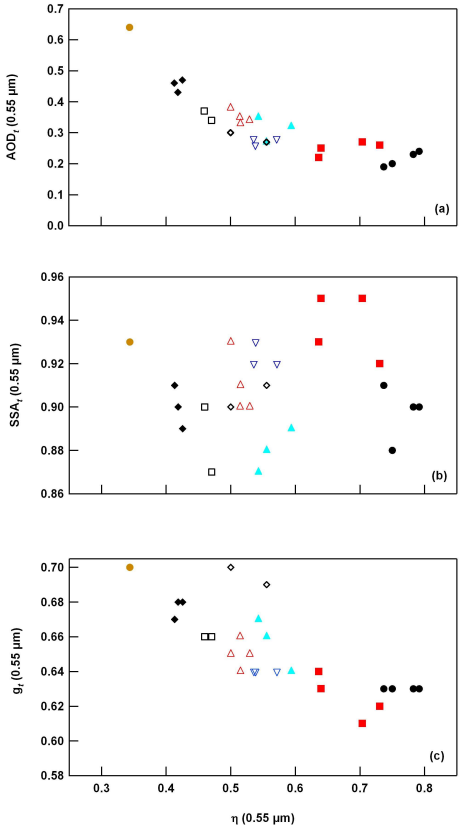

Fig. 7. Simulated values at 0.55 µm of **(a)** AOD_t, **(b)** SSA_t, and g_t as a function of η at 0.55 µm. Different symbols are used to characterize different dusty-days: 17 July 2003 (●); 24 July 2003 (△); 8 July 2004 (▽); 5 July 2005 (●); 6 July 2005 (■); 18 July 2005 (▲); 19 June 2006 (◆); 22 June 2006 (□); 26 June 2006 (◇).

ACPD
10, 20673–20727, 2010

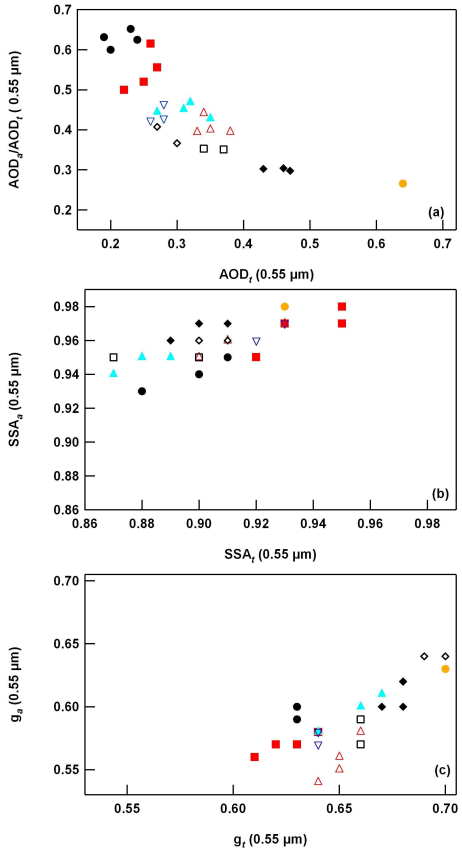

Fig. 8. (a) Ratios of the anthropogenic particle AOD (AOD_a) to the AOD by all particles (AOD_t) versus AOD_t. **(b)** SSA by anthropogenic particles (SSA_a) versus SSA_t. **(c)** Asymmetry parameter by anthropogenic particles (g_a) versus g_t. Different symbols are used to characterize different dusty-days: 17 July 2003 (●); 24 July 2003 (△); 8 July 2004 (▽); 5 July 2005 (✹); 6 July 2005 (■); 18 July 2005 (▲); 19 June 2006 (◆); 22 June 2006 (□); 26 June 2006 (✪).

ACPD
10, 20673–20727, 2010

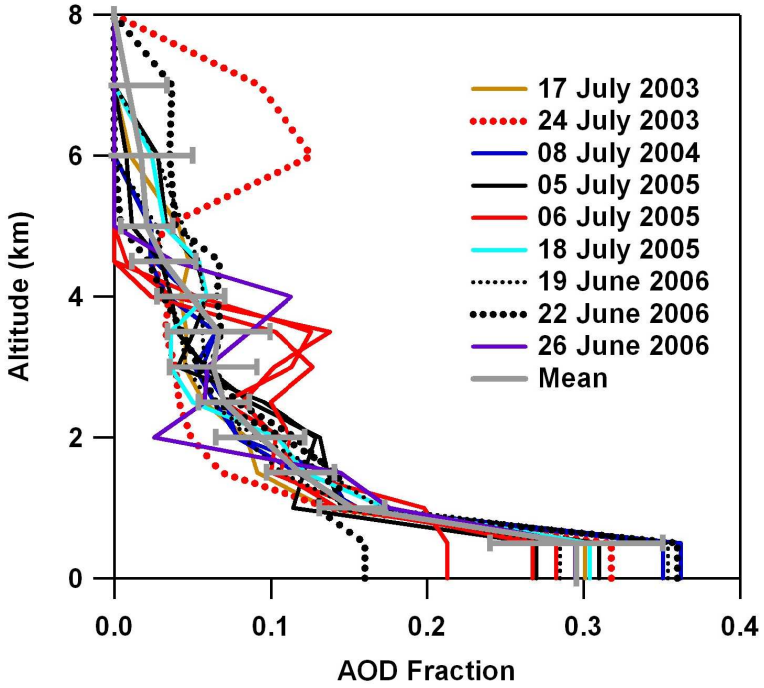

Fig. 9. Instantaneous dusty-day AOD fractions as a function of altitude. The solid grey line represents the mean vertical profile of the AOD fraction. Horizontal error bars represent ±1 standard deviation from the average value.

ACPD
10, 20673–20727, 2010

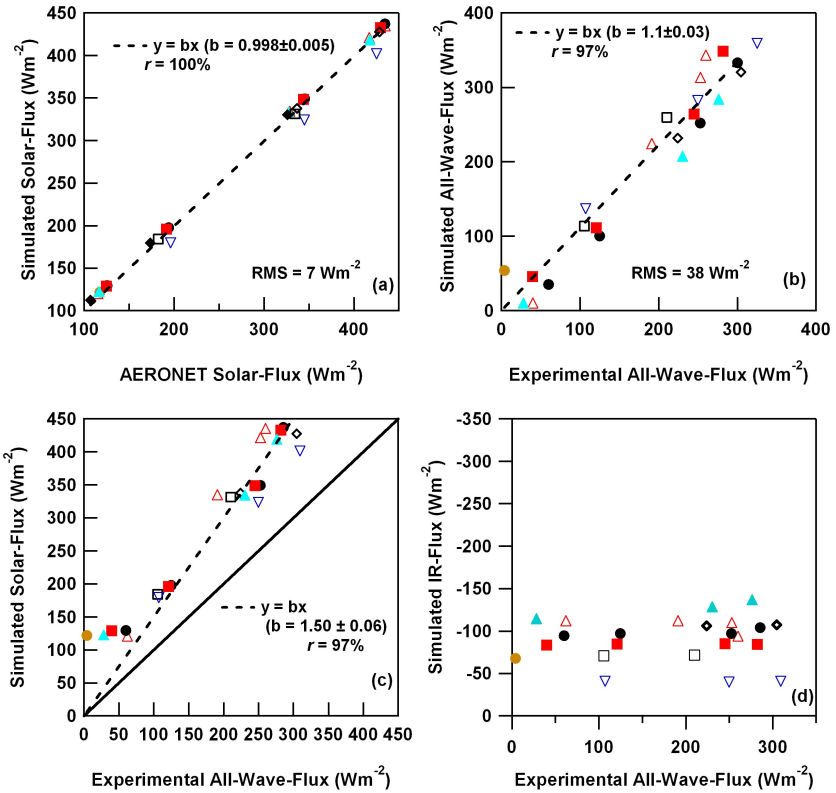

Fig. 10. (a) Simulated solar-fluxes versus AERONET solar-fluxes at the surface. Simulated **(b)** all-wave, **(c)** solar, and **(d)** IR fluxes versus experimental all-wave fluxes at the surface. Dotted lines represent least square fits. The solid line in Fig. 10c represents the 1:1 line. Different symbols are used to characterize different dusty-days: 17 July 2003 (●); 24 July 2003 (△); 8 July 2004 (▽); 5 July 2005 (●); 6 July 2005 (■); 18 July 2005 (▲); 19 June 2006 (◆); 22 June 2006 (□); 26 June 2006 (✪).

ACPD
10, 20673–20727, 2010

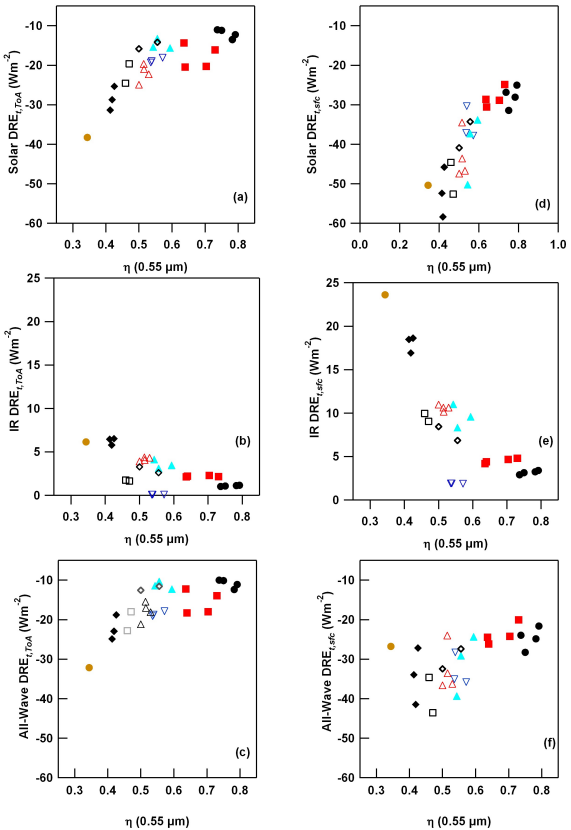

Fig. 11. ToA-DRE by all particles in the **(a)** solar, **(b)** IR, and **(c)** solar+IR spectral range as a function of the fine mode fraction η at 0.55 μm. sfc-DRE by all particles in the **(d)** solar, **(e)** IR, and **(f)** solar+IR spectral range as a function of η. Different symbols are used to characterize different dusty-days: 17 July 2003 (●); 24 July 2003 (△); 8 July 2004 (▽); 5 July 2005 (✹); 6 July 2005 (■); 18 July 2005 (▲); 19 June 2006 (◆); 22 June 2006 (□); 26 June 2006 (✪).

ACPD
10, 20673–20727, 2010

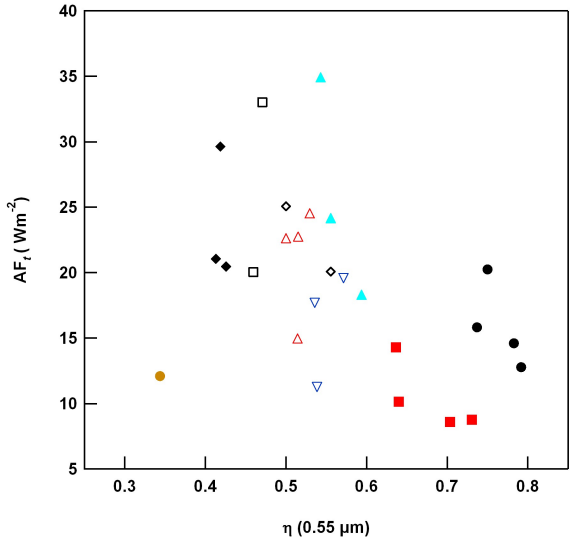

Fig. 12. Solar atmospheric forcing by all particles versus η at 0.55 μm. Different symbols are used to characterize different dusty-days: 17 July 2003 (●); 24 July 2003 (△); 8 July 2004 (▽); 5 July 2005 (●); 6 July 2005 (■); 18 July 2005 (▲); 19 June 2006 (◆); 22 June 2006 (□); 26 June 2006 (◇).

ACPD
10, 20673–20727, 2010

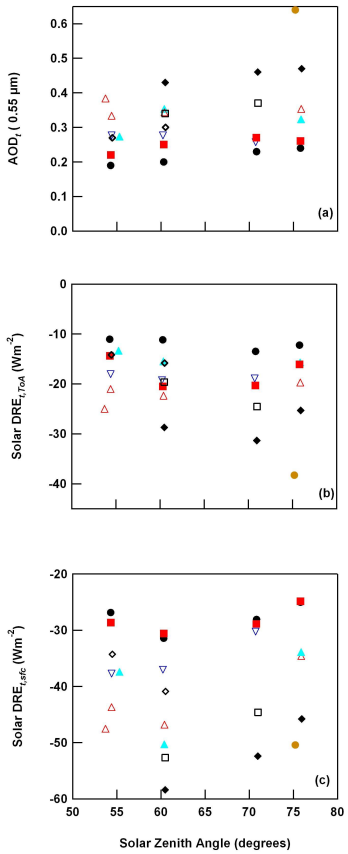

Fig. 13. **(a)** AOD at 0.55 µm, **(b)** solar ToA-DRE, and **(c)** solar sfc-DRE by all particles as a function of the solar zenith angle. Different symbols are used to characterize different dusty-days: 17 July 2003 (●); 24 July 2003 (△); 8 July 2004 (▽); 5 July 2005 (⬟); 6 July 2005 (■); 18 July 2005 (▲); 19 June 2006 (◆); 22 June 2006 (□); 26 June 2006 (◇).

ACPD
10, 20673–20727, 2010

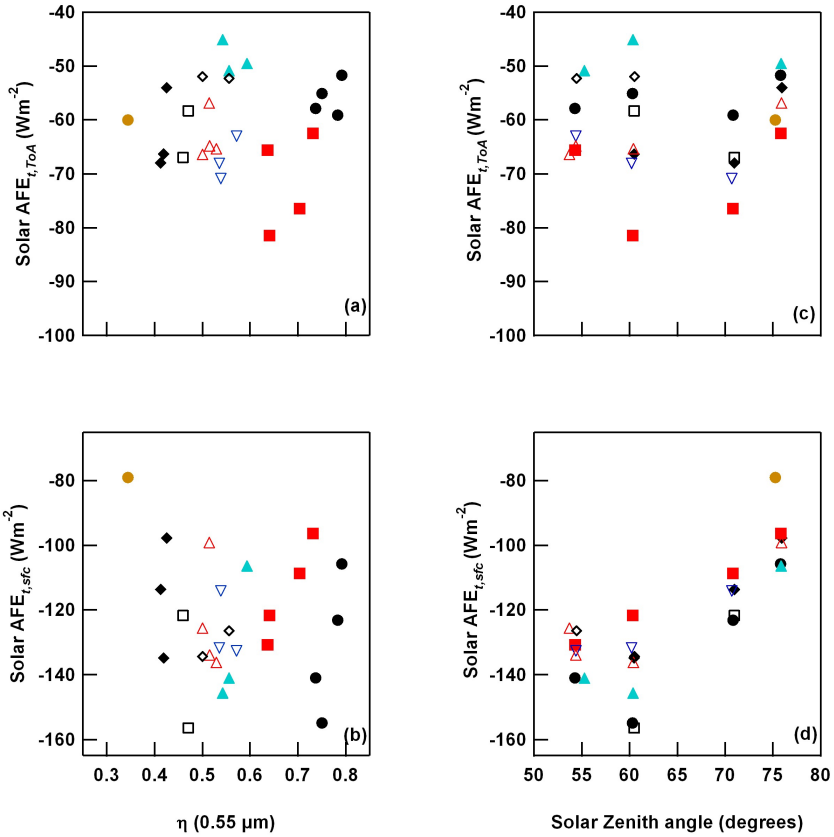

Fig. 14. Solar AFE by all particles versus η **(a)** at the ToA and **(b)** surface, and as a function of the solar zenith angle **(c)** at the ToA and **(d)** surface. Different symbols are used to characterize different dusty-days: 17 July 2003 (●); 24 July 2003 (△); 8 July 2004 (▽); 5 July 2005 (⬣); 6 July 2005 (■); 18 July 2005 (▲); 19 June 2006 (◆); 22 June 2006 (□); 26 June 2006 (◈).

ACPD
10, 20673–20727, 2010

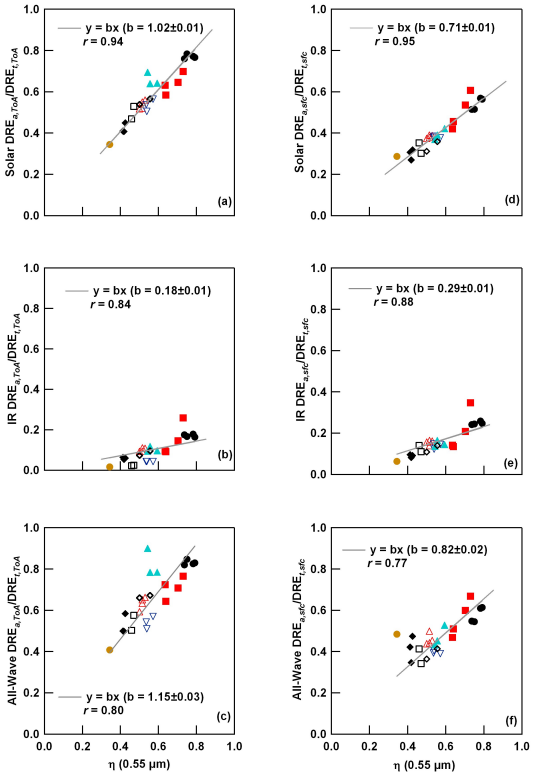

Fig. 15. Ratio of the DRE by anthropogenic particles (DRE_a) to the DRE by all particles (DRE_t) as a function of the fine mode fraction η **(a–c)** at the ToA and in the solar, IR, and solar+IR spectral range, respectively, **(d–f)** at the surface and in the solar, IR, and solar+IR spectral range, respectively. Different symbols are used to characterize different dusty-days: 17 July 2003 (●); 24 July 2003 (△); 8 July 2004 (▽); 5 July 2005 (⬢); 6 July 2005 (■); 18 July 2005 (▲); 19 June 2006 (◆); 22 June 2006 (□); 26 June 2006 (◘).

ACPD
10, 20673–20727, 2010